

AD-A017 729

NUMERICAL MODELING OF AURORA. VOLUME I OF THE  
CALENDAR YEAR 1974 ANNUAL REPORT TO THE DEFENSE  
NUCLEAR AGENCY. HAES REPORT NUMBER 16

Naval Research Laboratory

Prepared for:

Defense Nuclear Agency

October 1975

DISTRIBUTED BY:

**NTIS**

National Technical Information Service  
U. S. DEPARTMENT OF COMMERCE

336113

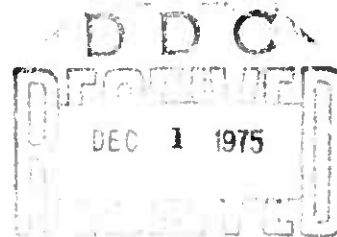
NRL Memorandum Report 3120

ADA 017729

**Numerical Modeling of Aurora**  
**Volume I of the Calendar Year 1974**  
**Annual Report to the Defense Nuclear Agency**  
**HAES Report No. 16**

*Plasma Dynamics Branch*  
*Plasma Physics Division*

October 1975



This research was sponsored by the Defense Nuclear Agency under Subtask L25AAXHX633,  
work unit 15, work unit title "Numerical Auroral Models."



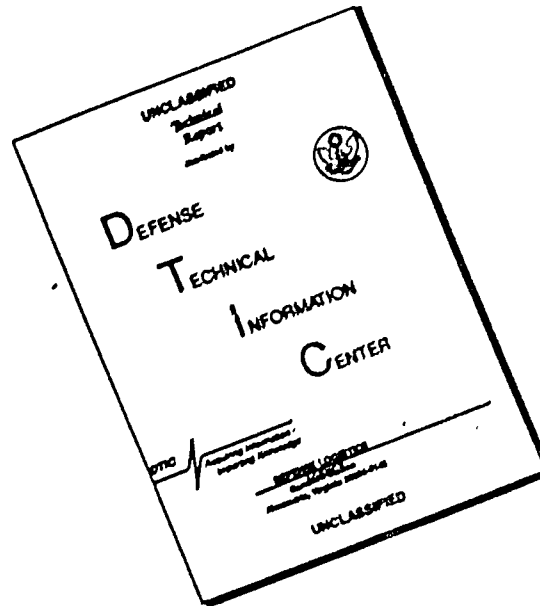
Reproduced by  
**NATIONAL TECHNICAL  
INFORMATION SERVICE**  
U.S. Department of Commerce  
Springfield, VA 22151

**NAVAL RESEARCH LABORATORY**  
**Washington, D.C.**

Approved for public release; distribution unlimited.

REPORT DOCUMENTATION PAGE		READ INSTRUCTIONS BEFORE COMPLETING FORM
1. REPORT NUMBER NRL Memorandum Report 3120	2. GOVT ACCESSION NO.	3. RECIPIENT'S CATALOG NUMBER
4. TITLE (and Subtitle) NUMERICAL MODELING OF AURORA -- Volume I of the Calendar Year 1974 Annual Report to the Defense Nuclear Agency -- HAES Report No. 16		5. TYPE OF REPORT & PERIOD COVERED Interim report on a continuing NRL problem.
		6. PERFORMING ORG. REPORT NUMBER
7. AUTHOR(s) Plasma Dynamics Branch Plasma Physics Division		8. CONTRACT OR GRANT NUMBER(s)
9. PERFORMING ORGANIZATION NAME AND ADDRESS Naval Research Laboratory Washington, D.C. 20375		10. PROGRAM ELEMENT, PROJECT, TASK AREA & WORK UNIT NUMBERS NRL Problem H02-35 DNA Subtask L25AAXHX633
11. CONTROLLING OFFICE NAME AND ADDRESS Defense Nuclear Agency Washington, D.C. 20305		12. REPORT DATE October 1975
		13. NUMBER OF PAGES 70
14. MONITORING AGENCY NAME & ADDRESS (if different from Controlling Office)		15. SECURITY CLASS. (of this report) UNCLASSIFIED
		15a. DECLASSIFICATION DOWNGRADING SCHEDULE
16. DISTRIBUTION STATEMENT (of this Report) Approved for public release; distribution unlimited.		
17. DISTRIBUTION STATEMENT (of the abstract entered in Block 20, if different from Report)		
18. SUPPLEMENTARY NOTES This research was sponsored by the Defense Nuclear Agency under Subtask L25AAXHX633, work unit 15, work unit title Numerical Auroral Models.		
19. KEY WORDS (Continue on reverse side if necessary and identify by block number) High Altitude Nuclear Explosion (HANE) phenomenology Aurora Auroral modeling Auroral chemistry		
20. ABSTRACT (Continue on reverse side if necessary and identify by block number) In support of High Altitude Nuclear Explosion (HANE) phenomenology the NRL Plasma Physics Division has developed theoretical models for many of the important features of the aurora. In this report we describe the auroral modeling results for the energy deposition of energetic elec- trons and ions (protons) in the atmosphere, the effects of the energy deposition on the chemistry of the auroral ionosphere, and the effects of auroral ionization on the electric fields and currents at high latitudes. These model results provide a valuable link between the existing and ongoing auroral measurements and the HANE phenomenology simulations.		

# DISCLAIMER NOTICE



THIS DOCUMENT IS BEST QUALITY AVAILABLE. THE COPY FURNISHED TO DTIC CONTAINED A SIGNIFICANT NUMBER OF PAGES WHICH DO NOT REPRODUCE LEGIBLY.

## CONTENTS

### Section 1

INTRODUCTION .....	1
--------------------	---

### Section 2

CHARGED PARTICLE ENERGY DEPOSITION .....	4
2.1 ELECTRON DEPOSITION: Continuous Slowing Down (CSD) Approximation .....	5
2.2 ELECTRON DEPOSITION: Transport Equation Approach ..	10
2.3 PROTON DEPOSITION .....	19

### Section 3

THE AURORAL CHEMISTRY CODE .....	26
----------------------------------	----

### Section 4

AURORA ARC MODELING .....	39
4.1 THE 2-D AURORAL ARC MODEL .....	39
4.2 EXTENDED AURORAL ARC MODELING .....	46

### Section 5

SUMMARY AND CONCLUSIONS .....	56
ACKNOWLEDGEMENT .....	61
REFERENCES .....	62

**Other Unclassified Volumes in This Series**

**Volume III -- "Post Stabilization Ionization Level Predictions," NRL Memorandum Report 3126, September 1975**

**Volume V -- "Electron Impact Excitation Parameters for Selected Nitrogen and Oxygen Transitions and for Other Helium-Like Ions for HANE Applications," NRL Memorandum Report 3133, September 1975**



NUMERICAL MODELING OF AURORA  
Volume I of the Calendar Year 1974  
Annual Report to the Defense Nuclear Agency  
HAES Report No. 16

Section 1

INTRODUCTION

A defensive policy, particularly one of limited retaliation, requires a thorough knowledge and understanding of the environment within which this policy may have to be implemented. An a priori knowledge of the environment is required to successfully define and deploy the intelligence gathering and communications links upon which such a posture must be based. As these systems become more complex, and as they are required to carry and impart more detailed information, they become more susceptible to the disturbances which would be created in a nuclear exchange.

The detonation of a high-altitude nuclear explosion (HANE), and even the detonation of lower altitude weapons with subsequent heave and lofting of weapon debris, can create large scale ionospheric disturbances. Whether these disturbances have as their source prompt gamma-ray, x-ray, UV, optical, or IR emission, or later decay betas or ionized debris, the net effect on upper atmosphere constituents is to ionize or excite these species. The influx of energy can initiate a complex series of chemical and physical reactions resulting in enhanced ionization levels, increased UV, optical and IR radiations, and perturbations of existing magnetic and electric fields. The net effect these perturbations will have on defensive systems must be thoroughly understood so that our defensive posture, or our ability to effectively retaliate, will not be seriously degraded.

Systems designers and analysts need to have detailed knowledge of HANE effects but must face the limitations of a test ban treaty. How can systems be effectively exercised or tested without resorting to actual nuclear tests? The only approach available is to model or simulate, first the HANE perturbations, and second, the effects of these perturbations on proposed systems. However, any large scale modeling or simulation effort at some point must touch base with reality. Confidence in predictions or conclusions based on the modeling increases as the validity of the model is established by quantitatively reproducing known conditions.

In modeling HANE phenomenology, one logical place to establish such validity and confidence, is in the aurora. These ionospheric disturbances, while not directly applicable to HANE phenomenology, have enough direct correlation in apparent observables to effectively help bolster confidence in our ability to model HANE disturbances. While the energetics of the emissions or particles creating the disturbances may be different and the ionization and heating levels considerably higher for a HANE, modeling either phenomenon requires a detailed understanding of (1) particle interactions, (2) all appropriate chemical reactions, and (3) potential changes or enhancements in ionospheric fields and currents.

These three areas have been addressed by the Plasma Dynamics Branch during the past year. The energetics of charged particle interactions has been approached from several directions. Electron energy deposition has been treated in a simplified form by assuming a continuous energy loss model with no pitch angle diffusion, and in a more detailed transport equation approach which takes into account pitch angle diffusion and allows for discrete large angle scattering events. A first step in understanding the interactions of protons, and heavier



debris ions, with the atmosphere was taken with the development of a continuous loss model similar to that developed for electrons.

An auroral chemistry code has been developed to permit an examination of upper atmospheric species and reaction rates. The code presently will accept an energy deposition profile from either of the above deposition models, and by tracking 14 different species is capable of generating both spatial and temporal profiles of selected species, ionization levels, emission rates, etc.

The third area of investigation involved the development of auroral arc models. We were concerned here with developing an understanding of the gross morphology of the currents, fields, and plasma densities found in auroral arcs (small scale structure is dealt with in Volume IV under plasma instabilities). Modeling the weakly ionized part of a UV fireball and the late-time motion (>5 minutes) of the nuclear disturbed ionosphere uses essentially the same relationships as those for modeling auroral arcs. The equations employed included continuity, momentum, and energy for electrons, ions, and neutrals, and an equation for the electrostatic potential.

The work performed at NRL during the past year in all three of these areas is summarized in the remainder of this volume. Much of this work has been previously reported in NRL Memo Reports, at several symposia, in technical journals, and at DNA sponsored meetings. The principal contributors in each technical area are listed as authors of the section describing that work.



## CHARGED PARTICLE ENERGY DEPOSITION

P.S. Julienne, D.C. Strickland, P.C. Kepple,  
J. E. Rogers III, and J. Davis

Agreeing that understanding natural auroral processes is quite useful to the prediction and understanding of nuclear disturbances, one must examine the source mechanisms for the aurora. It is understood that aurora are initiated and sustained by charged particle interactions in the upper atmosphere. The details of the interactions between impinging energetic electrons and protons, and the atoms and molecules of the atmosphere must be accurately modeled to permit a detailed understanding of the energy transport processes, chemical reactions, ionization levels, and radiative emissions initiated by these interactions. These same phenomena occur in the nuclear environment (Starfish electron patch, debris patch, etc.).

In this section we address the problem of modeling the deposition of energy in the atmosphere by energetic electrons and protons. These particles are directed into the atmosphere along magnetic field lines and deposit their energy in collisional processes with the atomic and molecular species present. Since both the total number and relative densities of these species are altitude dependent, the energy deposition profile is also altitude dependent. The collisional processes are interactions which can ionize the atmospheric constituents and impart kinetic energies. They therefore can initiate a complex set of chemical and transport processes.

Electron energy deposition has been approached from two directions. In the first, a simplified model is generated in which the discrete nature of electron interactions is ignored and the energy deposition is treated in a continuous manner. In the second, a detailed

accounting of discrete collisional processes is maintained in an attempt to create an "exact" model for electron energy deposition. Both models are discussed in this section and consideration is given to the constraints, limitation, and applicability of each model. The section terminates with a presentation of the model used to calculate proton energy deposition.

## 2.1 ELECTRON DEPOSITION: Continuous Slowing Down (CSD) Approximation

To study the qualitative, and to approximate the quantitative, features of atmospheric electron deposition, it is desirable to have a simple, fast running electron deposition code. To develop such a code we have used a generalized continuous slowing down scheme for the altitude dependent energy deposition (see Julianne [1974] for a complete treatment). Since the effect of pitch angle diffusion is not treated, the predicted electron penetration is overestimated and energy deposition at higher altitudes is underestimated. Given arbitrary input fluxes, the code is useful for comparing auroral energetics, relative excitation rates, integrated emission rates, and the secondary electron fluxes. It is fast running, simple, and requires only a knowledge of the electron inelastic collisional cross sections. The code calculates the volume production rates at each altitude for all included processes. One advantage of this code over previous codes is that it does not rely on analytical fits to the cross sections. The cross sections are represented in numerical form by relatively few points in a cubic spline interpolation scheme. Thus, experimental cross sections can be readily used where they are available.

The flux of energetic primary electrons,  $\phi$ , electrons  $\text{cm}^{-2} \text{sec}^{-1} \text{ev}^{-1} \text{ster}^{-1}$ , incident on the atmosphere in an aurora typically ranges in energy from 1 to 30 keV. The flux is assumed to be isotropic over the downward hemisphere (no magnetic field

effects), and the vertically incident flux is obtained by integrating the vertical flux component ( $\phi \cos \mu$ ) over azimuthial and pitch angles ( $\mu$  = pitch angle). This gives  $\pi\phi$  electrons per square centimeter, per second, and per eV vertically incident. To calculate the ionization and excitation levels of the atmosphere both the primary and secondary electrons must be considered. The secondary electrons, predominately with energies below several hundred volts, tend to be fairly isotropic and to lose their energy locally. The present code uses a continuous slowing down (CSD) approximation for both primary and secondary electrons.

The energy lost,  $dE$ , by electrons of energy,  $E$ , traveling a distance,  $dx$ , through a gas of uniform density,  $N$ , is

$$dE = N L(E) dx \quad . \quad (2.1)$$

The loss function,  $L(E)$ , is determined by the cross section for all inelastic collisions

$$L(E) = \frac{1}{N} \sum_{\alpha} N_{\alpha} \left\{ \sum_i W_{i\alpha} \sigma_{i\alpha}(E) + \sum_j \int_0^{\frac{E - I_{j\alpha}}{2}} W S_{j\alpha}(E, W) dW \right\} \quad . \quad (2.2)$$

The summation is over all species,  $\alpha$ , and over the excitation and ionization states for each species. In the first sum, the  $W_{i\alpha}$  represents the energies of discrete excitation including the ionization threshold. The second sum represents the creation of secondary electrons of energy  $W$  from the various ionization states. The energy differential cross section  $S_{j\alpha}(E, W)$  is normalized so that

$$\sigma_{j\alpha}(E) = \int_0^{\frac{E - I_{j\alpha}}{2}} S_{j\alpha}(E, W) dW \quad .$$

$\sigma_{j\alpha}$  represents the total ionization cross section into state  $j$ .

Once the electron flux is known, the production rate of some state  $i$  in species  $\alpha$  is simply

$$P_{i\alpha}(Z) = N_{\alpha}(Z) \int_{W_{i\alpha}}^{\infty} \phi(E) \sigma_{i\alpha}(E) dE \quad (2.3)$$

If  $\sigma_i$  represents an emission cross section for some atomic or molecular line then  $P$  is the emission rate of that line.

The code uses a very simple scheme to deposit the primary energy at any altitude  $z$ . The vertically incident flux,  $\phi$ , is divided into channels of energy  $E_n$  to  $E_{n+1}$ ,  $n = 1, 2, N$  for suitably chosen  $N$ . The flux in each channel is defined as

$$\phi_n = \int_{\frac{E_{n-1} + E_n}{2}}^{\frac{E_{n+1} + E_n}{2}} \phi(E) dE \text{ electrons cm}^{-2} \text{ sec}^{-1} \quad (2.4)$$

The incident flux is then treated as a series of  $n$  delta functions of strength  $\phi_n$ . Each delta function is deposited independently. The energy continuously degrades from its initial value  $E_n$  (at  $Z = Z_0$ ), to a value of  $E_n(Z)$  at altitude  $Z$ . Using these relationships and appropriate cross section values one may calculate the excitation rates from degraded primary electrons and the total secondary electron production rate spectrum, which is converted to a secondary flux using the CSD approximation. Similarly, the tertiary flux can be obtained. The procedure can be applied for any order of electrons. However, since it rapidly converges it is not necessary to go beyond quaternary electrons.

The cross sections currently used to calculate the loss function are shown in Table 2.1. They will be discussed in detail in a separate report. The cross sections are of two types: first, direct

TABLE 2.1

SUMMARY OF N<sub>2</sub>, O<sub>2</sub>, AND O CROSS SECTIONS

State	Reference
N <sub>2</sub> Ionization	Rapp and Englander-Golden [1965]; Schram et al. [1965].
A <sup>3</sup> Σ <sub>u</sub> <sup>+</sup>	Borst [1972].
B <sup>3</sup> Π <sub>g</sub>	Stanton and St. John [1969] ; Chung and Lin [1972].
C <sup>3</sup> Π <sub>u</sub>	Finn, Aarts, and Doering [1972]; Aarts and deHeer [1969].
W <sup>3</sup> Δ <sub>u</sub>	Chung and Lin, normalized to Chutjian et al [1973].
a <sup>1</sup> Π <sub>g</sub>	Ajello [1970](peak); Green and Stolarski [1972](high energy)
b <sup>1</sup> Π <sub>u</sub>	Green and Stolarski [1972].
b <sup>1</sup> Σ <sub>u</sub> <sup>+</sup>	Green and Stolarski [1972].
Rydbergs	Green and Stolarski [1972].
Vibration	Schulz [1964], normalized to Spence, Mauer, and Schulz [1972].
O <sub>2</sub> Ionization	Rapp and Englander-Golden [1965]; Schram et al. [1965].
a <sup>1</sup> Δ <sub>g</sub>	Linder and Schmidt [1971]; Trajmar et al. [1971].
b <sup>1</sup> Σ <sub>g</sub> <sup>+</sup>	Trajmar et al. [1971].

TABLE 2.1 (Con't)

State	Reference
6.1 eV	Green and Stolarski, normalized to Trajmar, et al. [1970].
$B^3\Sigma_u^-$	Green and Stolarski, normalized to Trajmar, et al.
9.9 eV	Green and Stolarski, normalized to Trajmar, et al.
Rydbergs	Green and Stolarski
O Ionization	Fite and Brackmann [1959].
$^1D$	Henry et al. [1969].
$^1S$	Henry et al. [1969].
$3s\ ^3S$	Zipf [1974].
$3s\ ^5S$	Zipf [1974].
Sum ( $\Delta l=1$ , $s=0$ )	Green and Stolarski
Sum ( $\Delta s=1$ )	Green and Stolarski
Sum ( $\Delta l=0$ , $s=0$ )	Green and Stolarski

electron impact cross sections for important states which can be used directly in calculation of the loss function; second, cross sections which are known for specific processes i.e., optical excitation functions for particular emission lines, including the effect of cascading. These cross sections are not used in the loss function but do permit the calculation of production rates for specific transitions.

Figure 2.1 shows a calculated secondary electron flux at altitudes of 200 and 105 kilometers for an incident 10 keV electron beam with unit flux. The dotted lines show the sum of up and down fluxes from Banks et al. [1974] for the same conditions. The peak deposition for Banks et al. is at 105 kilometers and is at 102 kilometers for the present calculations. The fluxes for the two calculations are similar below 100 keV. Both calculations show that the secondary flux is only weakly dependent on altitude. The continuous slowing down model appears to give a reasonable representation of the secondary electron flux over a wide altitude range.

## 2.2 ELECTRON DEPOSITION: Transport Equation Approach

In modeling electron energy deposition with this formulation, we (see Strickland et al. [1974] for more details) attempt to account for the discrete nature of the collisional processes, in particular, large angle scattering is allowed and the flux thus transported is accounted for. The form of the equation used is

$$\mu \frac{d\phi}{d\tau}(\tau_E, E, \mu) = -\phi(\tau_E, E, \mu) + S(\tau_E, E, \mu) \quad (2.5)$$

where  $\phi$  is the electron flux and  $S$  is the source function with both energy and angular dependence. The source function is defined as

$$S(\tau_E, E, \mu) = S_0(\tau_E, E, \mu) + \int G(E, E', \mu, \mu') \phi(\tau_E, E', \mu') dE' d\mu' \quad (2.6)$$



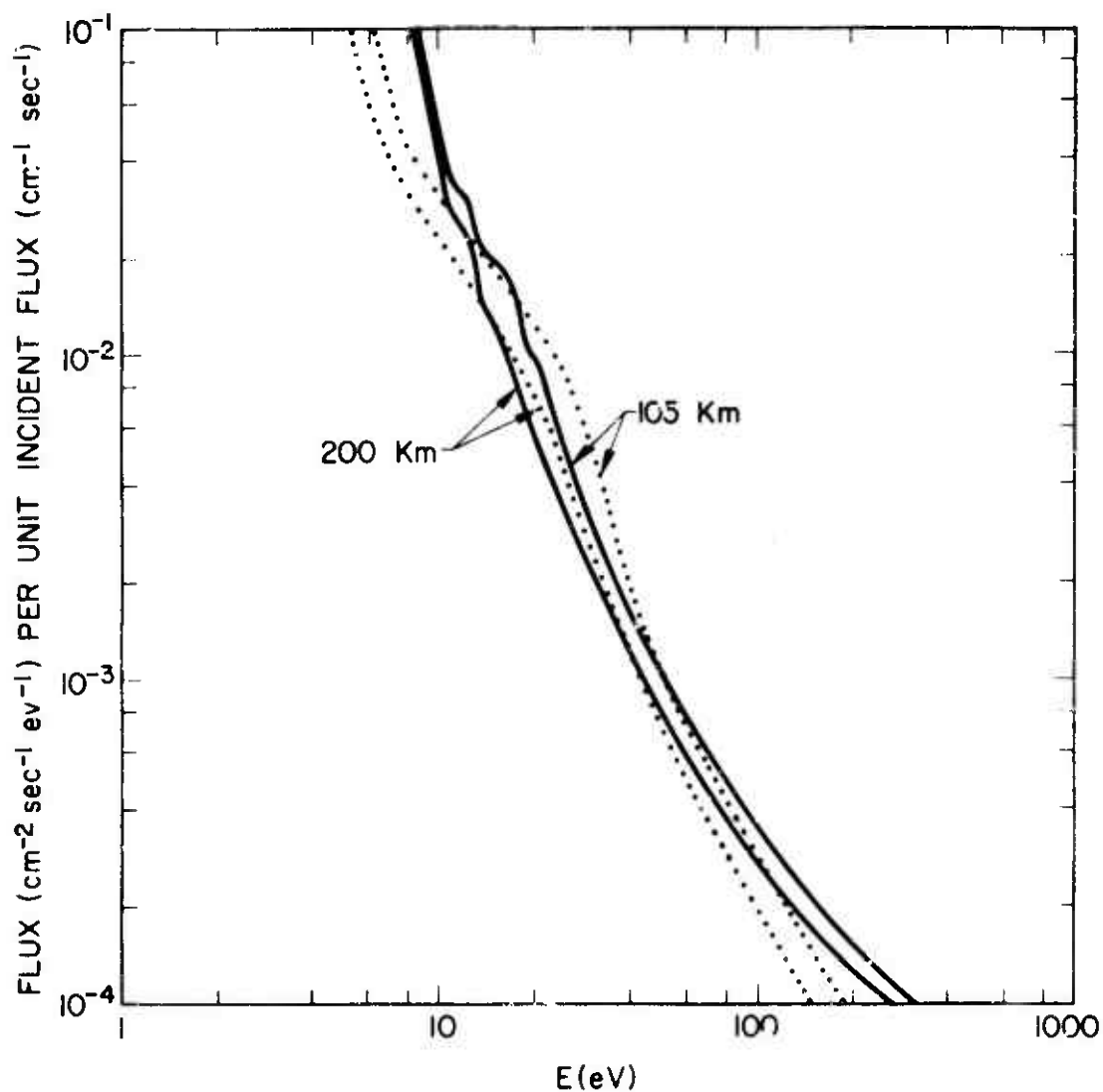


Fig. 2.1 — Low energy electron flux at 200 and 105 km from a unit incident flux (1 electron cm<sup>-2</sup> sec<sup>-1</sup>) of 10 dev electrons. The solid lines are from the present calculation and the dotted lines are from Banks et. al.

The term  $S_0$  is the initial source function, or driving term, in the equation.  $G$  is the redistribution function accounting for elastic and inelastic scattering. The terms in  $G$  are given in Strickland and Kepple [1974]. The independent variables are  $E$  the kinetic energy of the electron,  $\mu$  the cosine of the pitch angle, and  $\tau_E$  the optical depth for an electron of energy  $E$ . The optical depth in differential form is given by

$$d\tau_E = n(z) \left[ \sigma_e(E) + \sum_k \sigma_k(E) \right] dz \quad (2.7)$$

where  $\sigma_e$  is the elastic cross section, and  $\sigma_k$  is the  $k$ th inelastic cross section. The sum includes ionization cross sections. The present formulation of optical depth assumes a one-constituent atmosphere.

The source function represents the incident flux at the upper boundary of the atmosphere. Production of electrons within the atmosphere due to this energy source is accounted for in the integral term rather than in the source term. Equation (2.5) is solved in a matrix formulation. The matrix elements are calculated by approximating  $\phi$  quadratic in the logarithm of  $E$ , and linear in  $\mu$  within a given energy/pitch angle cell. An iterative procedure is required to calculate backscattered fluxes. The solution converges in as few as three or four iterations using a scheme which projects the iterated fluxes to their final values.

The term in the redistribution function,  $G$  (Equation (2.6)), accounting for elastic scattering is expressed as

$$G_e = \frac{1}{\sigma_T(E)} \sigma_e(E') \delta(E - E') p_e(E, \mu, \mu') \quad , \quad (2.8)$$

where  $p_e$  is the elastic angular redistribution function normalized in  $\mu$ ,

$$p_e = \frac{1}{\sigma_e(E)} \int_0^{2\pi} \frac{d\sigma_e}{d\Omega}(\theta) d\phi \quad (2.9)$$

$d\sigma_e/d\Omega$  is the differential elastic cross section which is assumed to take the form of the non-relativistic screened Rutherford cross section,

$$\frac{d\sigma_e}{d\Omega} = \frac{z^2 e^4}{4E^2} \frac{1}{(1 - \cos\theta + 2\eta)^2} \quad (2.10)$$

$\theta$  is the scattering angle and  $\eta$  is a screening parameter. The energy dependence of  $\eta$  is taken from Berger et al. [1970]. The program currently allows for a cutoff  $\theta_c$  beyond which scattering is not permitted. This allows us to determine the importance of large angle scattering relative to multiple small angle scattering and to make a more comprehensive comparison with Fokker-Planck results.

The Fokker-Planck equation can be obtained by expanding the integrand in Equation (2.6) in a Taylor series. Before doing this, we rewrite Equation (2.5) in a form more convenient for this expansion:

$$\mu \frac{d\phi}{dz}(z, E, \mu) = -n(z) \sigma_T(E) \phi(z, E, \mu) + n(z) \int \sigma(\Delta E, E + \Delta E, \theta) \cdot \phi(z, E + \Delta E, \mu + \Delta \mu) d\Delta E d\Delta \mu \quad (2.11)$$

where  $z$  is the distance along the field lines,

$$\begin{aligned} \Delta E &= E' - E, \\ \Delta \mu &= \mu' - \mu, \end{aligned}$$

and  $\sigma$  is the sum of all differential cross sections in  $\text{cm}^2 \text{ev}^{-1} \text{ster}^{-1}$ . The source term  $S_0$  has been dropped from Equation (2.5) for the

purposes of this discussion. The integrand,  $\sigma\phi$ , is now obtained by expanding about  $E$  and  $\mu$  to second order, giving:

$$\begin{aligned}\sigma'\phi' = & \sigma\phi - \frac{\partial}{\partial\mu}(\sigma\phi)\Delta\mu - \frac{\partial}{\partial E}(\sigma\phi)\Delta E + \frac{1}{2}\frac{\partial^2}{\partial\mu^2}(\sigma\phi)\Delta\mu^2 \\ & + \frac{1}{2}\frac{\partial^2}{\partial E^2}(\sigma\phi)\Delta E^2 + \frac{\partial^2}{\partial\mu\partial E}(\sigma\phi)\Delta\mu\Delta E\end{aligned}\quad (2.12)$$

where

$$\sigma'\phi' = \sigma(\Delta E, E + \Delta E, \theta)\phi(z, E + \Delta E, \mu + \Delta\mu) \quad \text{and}$$

$$\sigma\phi = \sigma(\Delta E, E, \theta)\phi(z, E, \mu) \quad .$$

Inserting Equation (2.12) into Equation (2.11), we obtain the Fokker-Planck equation:

$$\begin{aligned}\mu \frac{d\phi}{dz} = & - \frac{\partial}{\partial\mu} \phi \langle \Delta\mu \rangle - \frac{\partial}{\partial E} \phi \langle \Delta E \rangle + \frac{1}{2} \frac{\partial^2}{\partial\mu^2} \langle \Delta\mu^2 \rangle \\ & + \frac{1}{2} \frac{\partial^2}{\partial E^2} \phi \langle \Delta E^2 \rangle + \frac{\partial^2}{\partial\mu\partial E} \phi \langle \Delta\mu\Delta E \rangle\end{aligned}\quad (2.13)$$

where each of the diffusion coefficients  $\langle X \rangle$  is given by

$$\langle X \rangle = n(z) \int \sigma(\Delta E, E, \theta) X d\Delta E d\Omega \quad . \quad (2.14)$$

Equation (2.13) can be found in Walt et al. [1967], where they have dropped the last two terms as being small second order ones. A complete derivation of the diffusion coefficients for Equation (2.13) can be found in Strickland et al. [1974].

The status of auroral electron energy deposition codes was recently reviewed in a DNA sponsored meeting (June 14, 1974) where the code work by various contractors was compared. Participants in this meeting included Naval Research Laboratory, Lockheed Missiles and Space Co. (LMSC), Mission Research Corporation (MRC) and Visidyne. The several contractors were asked to supply calculated energy deposition rates for an incident flux with an energy dependence of the form

$$\phi_0(E) = \exp(-E(\text{keV})/10) \quad . \quad (2.15)$$

This flux is assumed isotropic at a 250 km upper boundary of a CIRA (1965) model atmosphere. The calculations began at 50 keV.

Figure 2.2 shows several calculated energy deposition rates using the above flux and several assumed cutoff angles in Equation (2.10). For these particular results, our set of  $N_2$  cross sections were applied to the sum of the three atmospheric constituents. As the cutoff value of the scattering angle is decreased, the expected trend develops, i.e., deeper penetration of the electron flux and lower loss rates at high altitudes.

The transfer results for  $\theta_c = 180^\circ$  are given in Figure 2.3 together with three other results. The LMSC curve is the Fokker-Planck result by M. Walt, the MRC curve is based on a modified continuous slowing down approach (incorporating pitch angle diffusion) by Tarr et al. and the BSM curve is a Monte Carlo result by Berger et al. [1974]. The transfer result in this figure is not identical to

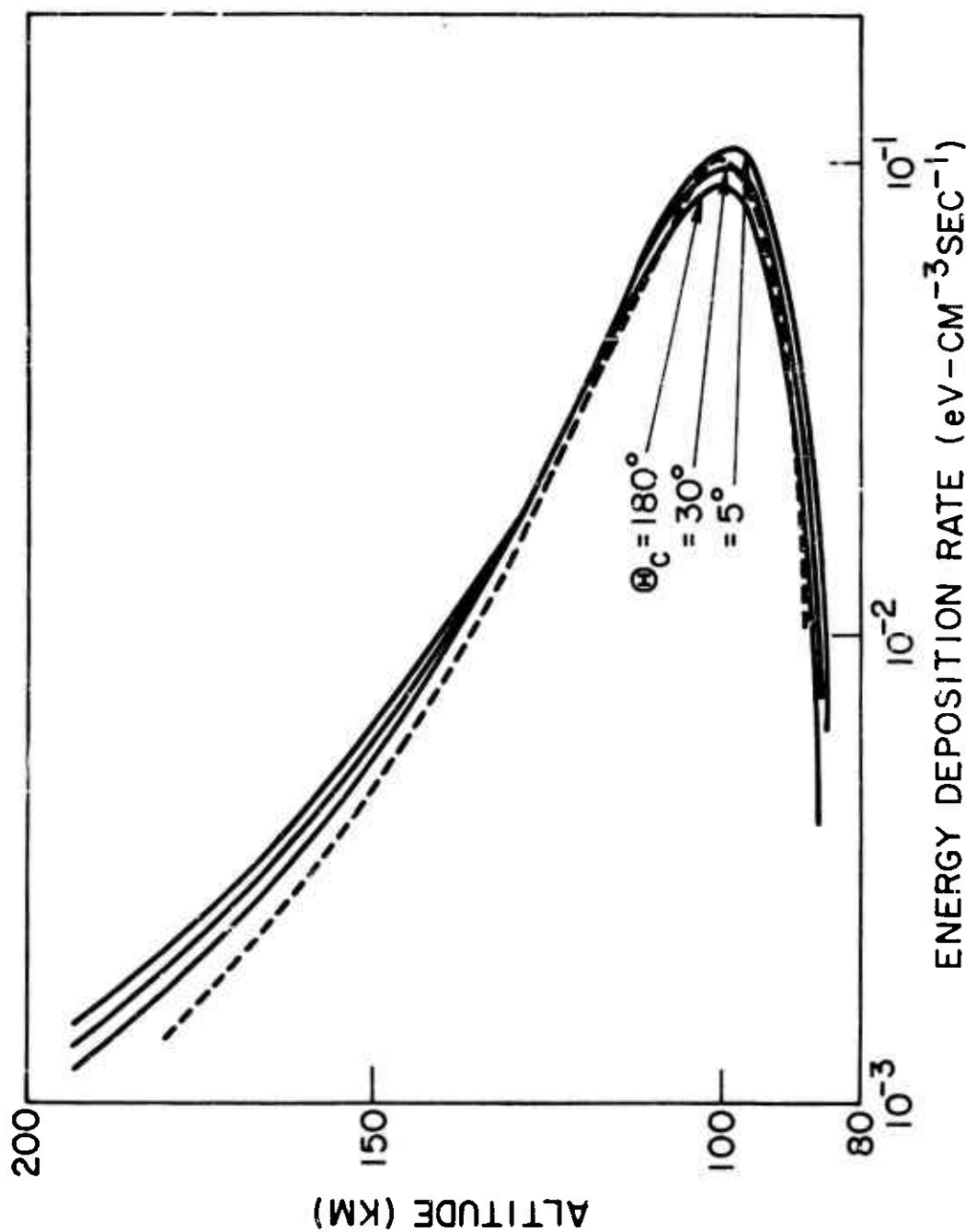


Fig. 2.2 — Calculated energy deposition rates for a flux defined by  $\phi = \exp(-E(\text{kev})/10)$ , with selected limits on allowed electron angular scattering (equation 2.10). The dashed curves are results by Walt, et. al. for the same incident flux

that for  $\theta_c = 180^\circ$  in the previous figure. The three atmospheric constituents were treated explicitly in this last calculation. There is good overall agreement between the various methods used to treat electron energy deposition. Of the differences that do exist between our results and the others, the trend in Figure 2.2 suggests that they are due, at least in part, to our more detailed treatment of angular scattering.

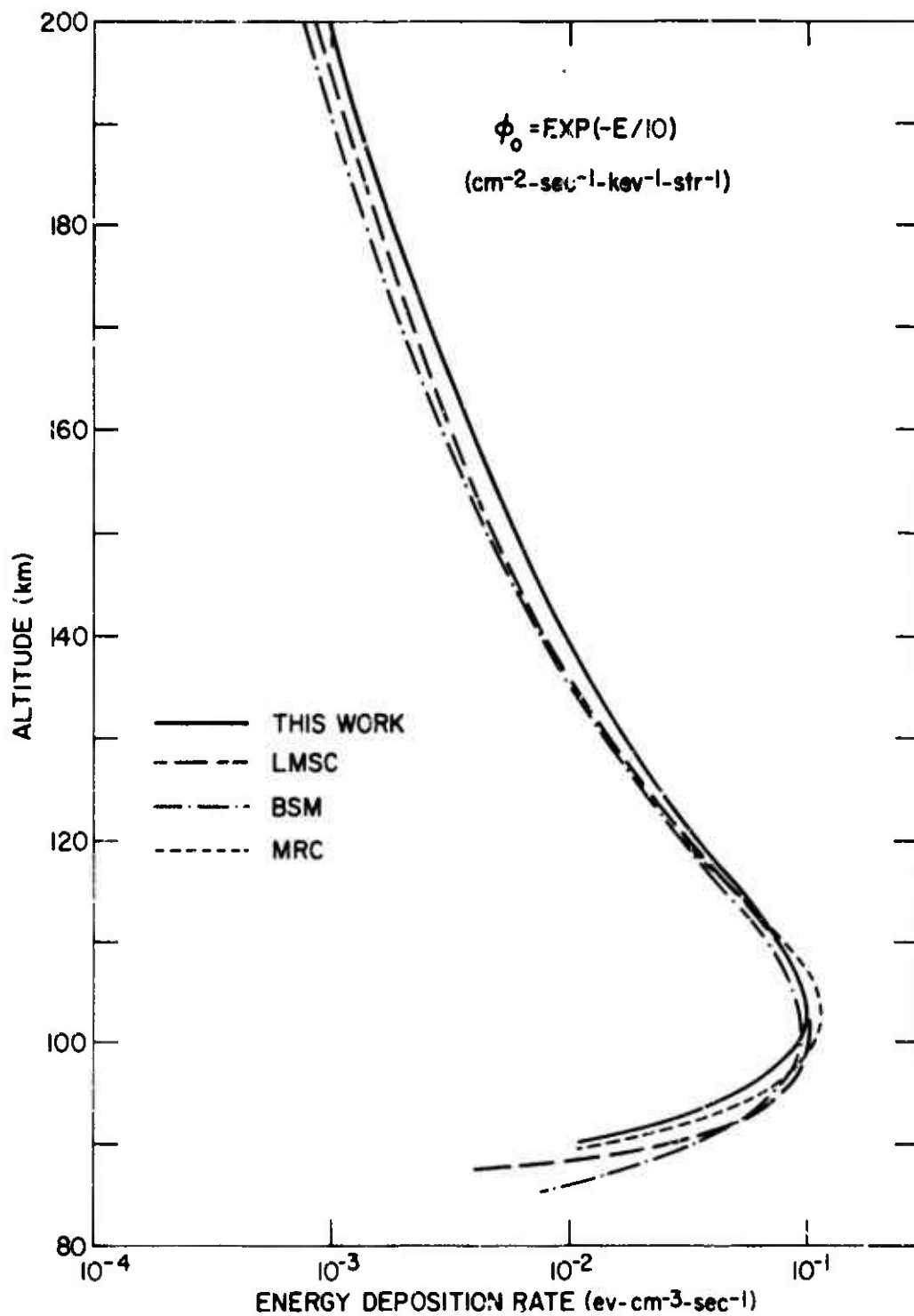


Fig. 2.3 — A comparison of several predicted energy deposition rates for the same incident flux. Note that there is good agreement between these results, within a factor of two, over all altitudes above 90 km.



### 2.3 PROTON DEPOSITION

In addition to energetic electrons, other particles, such as protons, are known to play significant roles in the creation of natural aurora. For example, hydrogen emissions observed in auroral displays can be explained by protons becoming excited hydrogen atoms through charge exchange processes with the atmospheric molecules. The modeling of proton energy deposition can be both simpler and more complicated than that of electron energy deposition. As charged particles, the protons and electrons are constrained to spiral around magnetic field lines in the earth's atmosphere. However, through charge exchange processes an energetic proton can become an excited hydrogen atom and in this uncharged state can readily cross field lines. NRL's goal in modeling proton energy deposition is to develop a simplified model which will be a useful first step in understanding and qualitatively predicting the altitude dependent volume production rates of the various ionized and excited states of the atmospheric species. To calculate these rates, a model for the energy loss and resulting slowing down of the incident proton is needed. The scheme adopted by NRL is the continuous slowing down approximation (CSDA)(described in detail in Rogerson and Davis [1974]). Effects due to the earth's magnetic field are neglected and the model is one-dimensional.

Peterson [1969] has shown that the CSDA works very well for electrons if their energy is sufficiently large that the energy loss in a single process is a small fraction of the original energy. Another limitation required by Peterson is that a large number of processes with widely distributed thresholds be included.

In the model generated here proton energies of 1 keV or larger are considered whereas the excitation and ionization processes have thresholds of the order of 10 eV. Hence in any single process the ratio of threshold to incident energy is small. In view of this, and because many processes with a wide range of thresholds are used in the proton loss function, the CSDA should be a reasonable approximation for the altitude dependent energy deposition of protons. Comments made on the limited applicability of the CSDA for electrons apply equally to the treatment here for protons, i. e., the code will predict too much penetration and will ignore backscatter. However, it is a relatively simple and fast running code and will be useful for analyzing and comparing the same processes as the electron CSD code. The effects of hydrogen atoms created by charge exchange are included by using the charge exchange formalism due to Allison [1958]. Secondary electron effects are treated by a scheme due to Julienne [1974].

In the CSDA, instead of undergoing discrete energy losses, the proton losses are modeled in a continuously varying process. Energy loss is described by

$$dE = -N(Z) L_p(E) dZ \quad (2.16)$$

where  $E$  is the proton energy,  $N(Z)$  is the local density of the atmosphere at altitude  $Z$ , and  $L_p(E)$  is the proton loss function for energy loss per unit of length per molecule in the vertical direction. For simplification only  $N_2$  is presently included as an atmospheric constituent. The 1965 Jacchia [1965] model atmosphere is used in this calculation.

The basic proton ( $H^+$ ) reactions with  $N_2$  that are included in the loss function are direct ionization of  $N_2$ , charge exchange ionization of  $N_2$  (creating a hydrogen atom), excitation of  $N_2$ , and elastic

scattering. The hydrogen atom created by charge exchange processes can undergo direct ionization of  $N_2$ , excitation of  $N_2$ , electron stripping of the hydrogen atom in collision with  $N_2$  and elastic scattering. It is assumed that an initially pure incoming proton flux becomes a charge equilibrated mixture of  $H^+$  and  $H$  resulting from the charge changing reactions. For a complete description of all terms in the proton loss function  $L_p(E)$  of Equation (2.10) the reader is referred to Rogerson and Davis [1974].

Figure 2.4 displays a number of total  $N_2^+$  production versus altitude curves calculated with the CSDA. The plots all have roughly the same shape. The 500 keV deposition curve produces fewer  $N_2^+$  ions than the 10 keV and 50 keV curves at higher altitudes and crosses over and exceeds these curves at lower altitudes. This is because charge exchange is essentially turned off at 500 keV and the total cross section for  $N_2^+$  production is lower than at 10 or 50 keV. As expected, the altitude of peak  $N_2^+$  creation decreases with increasing proton energy.

Figure 2.5 shows the contributions from the various ion producing reactions to total  $N_2^+$  production for an incident 100 keV proton flux. At higher altitudes, direct ionization by protons and ionization by electrons are dominant; at lower altitudes, where the proton has lost energy, charge exchange and atom ionization become more prominent until they actually dominate at the altitude of peak  $N_2^+$  production.

Figure 2.6 shows the secondary electron flux at a number of altitudes for the same 100 keV proton flux. These curves have roughly the same shape and appear to be typical of secondary electron distribution (EMG 13). The curve at 105.5 kilometers represents the secondary electron flux generated near the peak  $N_2^+$  production.

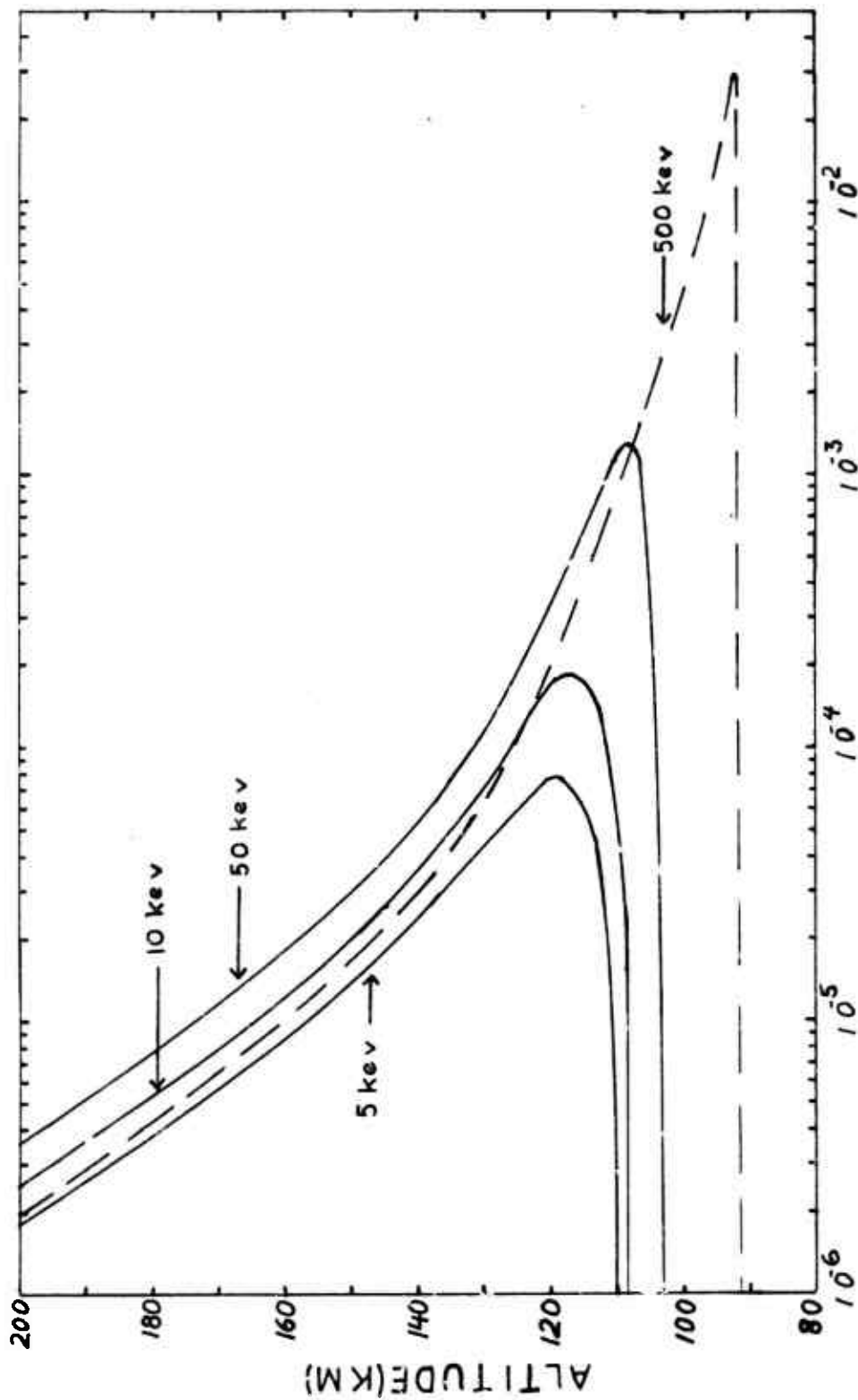


Fig. 2.4 - Total volume production rate of  $\text{N}_2^+$  for selected incident proton energies.

As expected, the altitude of peak  $\text{N}_2$  creation decreases with increasing proton energy.

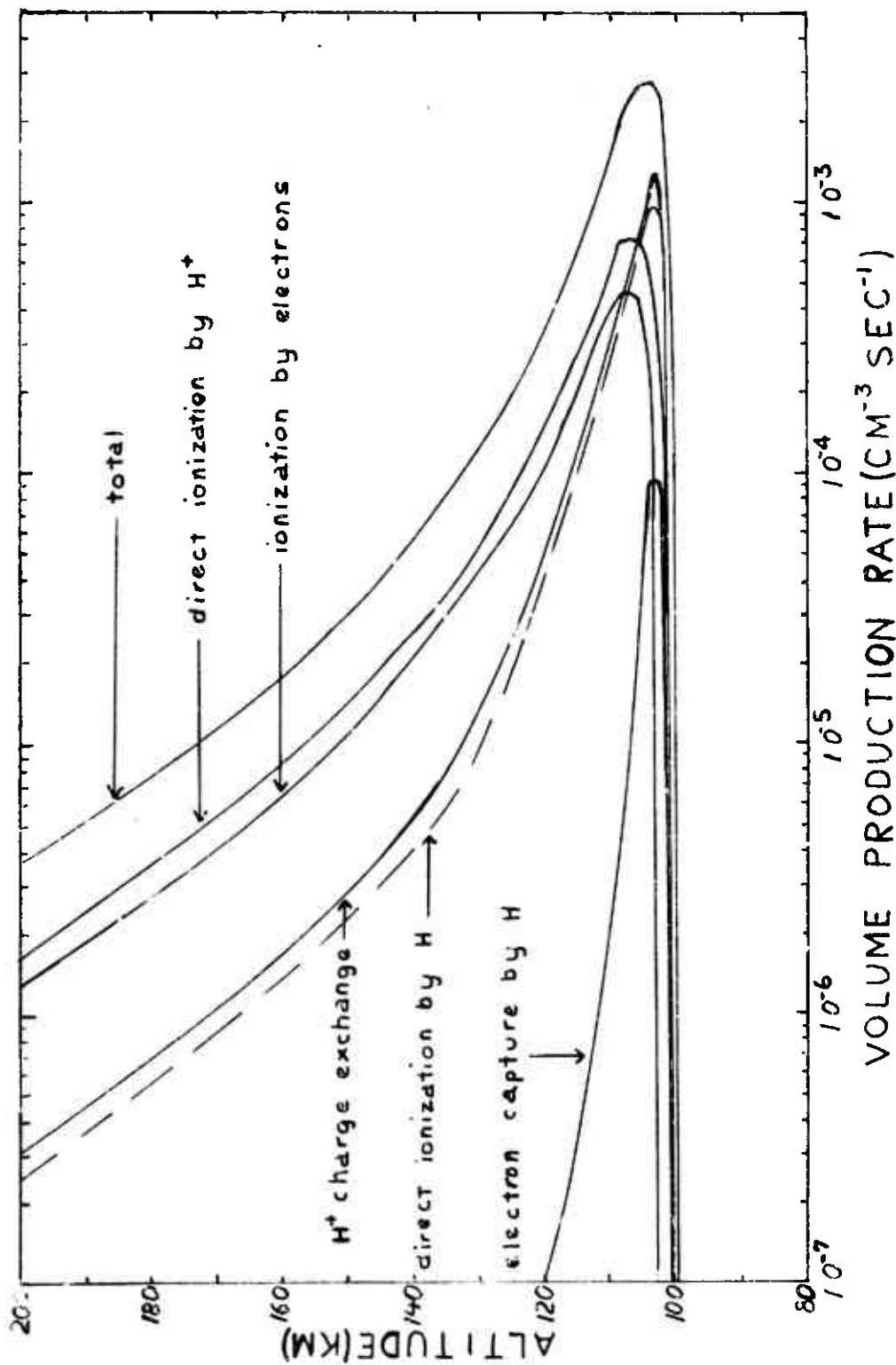


Fig. 2.5 — Contributions to total  $\text{N}_2^+$  production from various ion producing reactions for an incident 100 kev proton flux

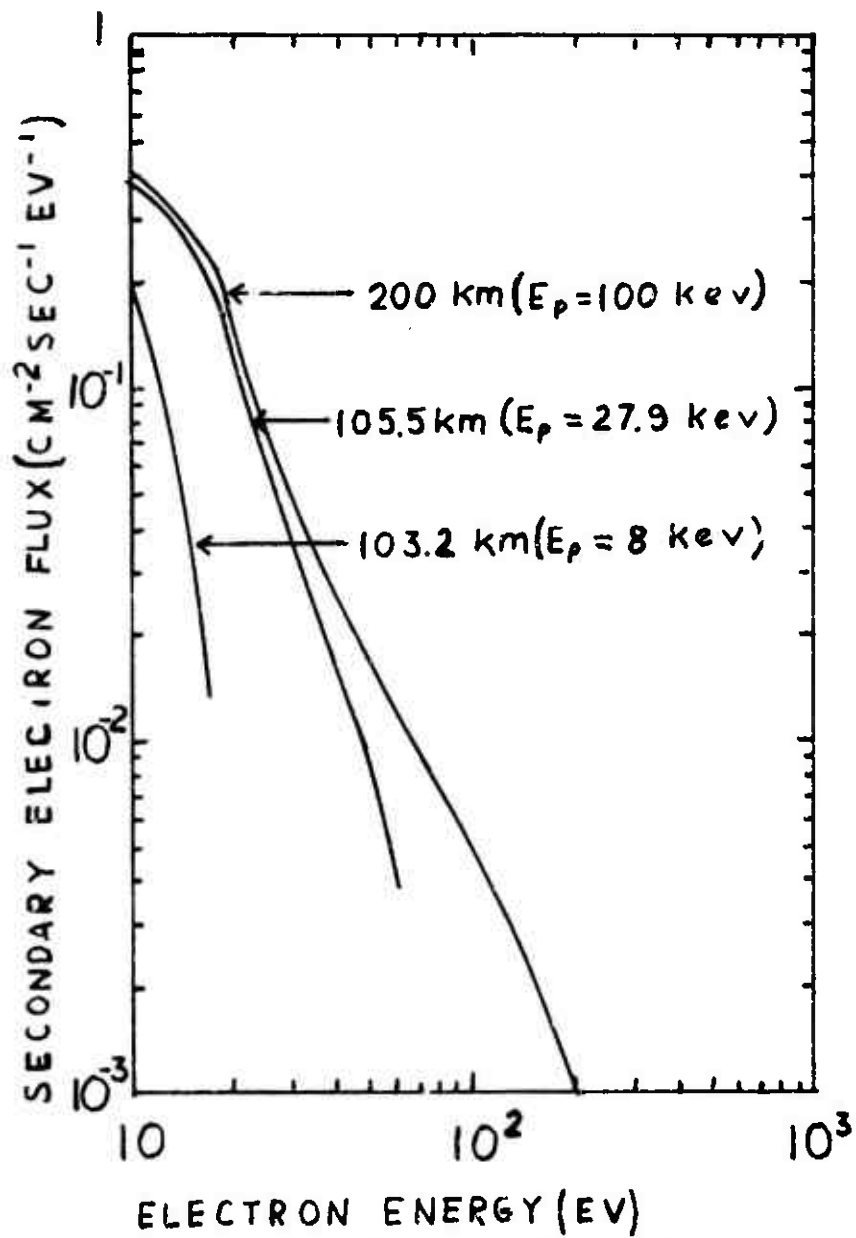


Fig. 2.6 -- Calculated secondary electron fluxes at selected altitudes for an incident 100 keV proton flux. The curve at 105.5 km represents the flux near the peak  $\text{N}_2^+$  production.

The model and results shown here are only the first step in understanding the basic physical mechanisms and energy partition among the various ionization levels in a proton aurora. Because of the simplicity of the model the volume production rates are probably underestimated and depths of penetration are probably overestimated. Planned future code improvements include: (1) using a distribution of proton energies rather than delta function energies; (2) adding O<sub>2</sub> and O to the atmosphere; and (3) introducing the earth's magnetic field. Also desirable at this time would be a comparison between the results of this code and other code work modeling proton energy deposition and a comparison between experimental data acquired on events such as PCA's with the results of this code. In the near future, the results for proton deposition will be extrapolated to heavier ions such as HANE debris patch particles.

### Section 3

#### THE AURORAL CHEMISTRY CODE

E. Hyman, P.S. Julianne, and D.F. Strobel

During the past year, NRL has developed a computer code to model the chemistry in the atmosphere during and subsequent to energy deposition by auroral electrons (see Hyman [1974]). The code is capable of generating altitude profiles for 14 atmospheric species as a function of time and for any given incident electron spectrum. The code can predict volume and column emissions of selected UV, visible, and IR spectral lines.

AURORA is a one-dimensional code that models the chemistry in the upper atmosphere after onset of auroral precipitation. The production rates for auroral processes are calculated with the electron deposition code described in Section 2.1. The processes included in the code are ionization, dissociation, and dissociative ionization of  $N_2$  and  $O_2$ , and ionization of O, all by electron impact. Additionally, a number of excitation processes in each of these species are monitored. A list of the electron production rates included in AURORA and the references for these rates are given in Table 3.1. Fourteen atmospheric species are tracked by AURORA. The production rates can be scaled up or down to simulate aurora of varying strengths for any given spectrum of incident electrons, and they can be turned on or off to observe the transient response of the atmosphere to auroral precipitation.

In the altitude regime between 100 and 150 kilometers, where most of the energy deposition occurs, 7 of the 14 species tracked have short equilibration time constants. Since we are not primarily concerned with processes occurring on a short time scale (approximately 1 second or less) these species are not integrated but are



Table 3.1  
ELECTRON PRODUCTION RATE

$N_2$	Reference
Vibrational	Shulz [1964] normalized to Spence, Mauer and Shulz [1972].
$A^3_u$ (Vegard-Kaplan)	Borst [1972].
$B^3_{\pi_g}$ (First-positive)	Stanton, St. John [1969] joined to Chung and Lin [1972].
$C^3_{\pi_u}$ (Second-positive)	Finn, Aarts, Doering [1972]; Aarts and DeHeer [1969].
$W^3_{\Delta_u}$	Shape of Chung and Lin [1972]; normalized to Chutjian, Cartwright and Trajmar [1973].
$a^1_{\pi_g}$ (Lyman-Birge-Hopfield)	Ajello [1970] (peak) and Green and Stolarski [1972] (high energy).
$b^1_{\pi_u}$	Green and Stolarski [1972].
$b'^1_{\Sigma_u^+}$	Green and Stolarski [1972].
$c^1_{\pi_u}$ ] Rydbergs	Green and Stolarski [1972].
$c'^1_{\Sigma_u^+}$ ]	Green and Stolarski [1972].
Ionization	Rapp and Englander-Golden [1965]; Schram, deHeer, VanderWiel and Kistenaker [1965].
Ratio 3914/Ionization	Stanton and St. John [1969]; Srivastava and Mirza [1968].

Table 3.1 (Continued)

O <sub>2</sub>	Reference
$a^1\Delta_g$	Trajmar, Cartwright and Williams [1971]; Linder and Schmidt [1971].
$b^1\Sigma_g^+$	Trajmar, Cartwright and Williams [1971]
6.1 ev peak	Green and Stolarski [1972], normalized to Trajmar, Williams and Kuppermann [1971].
$B^3\Sigma_u^-$ (Schumann-Runge)	Green and Stolarski [1972], normalized to Trajmar, Williams and Kuppermann [1971].
9.9 ev peak	Green and Stolarski [1972], normalized to Trajmar, Williams and Kuppermann [1971].
Rydbergs	Green and Stolarski [1972].
Ionization	Rapp and Englander-Golden [1965]; Schram, deHeer, vanderWiel and Kistenaker [1965].
Ratio $b^4\Sigma^-$ /ionization	Borst and Zipf [1970].
O	Reference
$1D$	Henry, Burke and Sinfailam [1969].
$1S$	Henry, Burke and Sinfailam [1969].
$3s^3S$ (1304)	Zipf (private communication)
$3s^5S$ (1356)	Zipf (private communication)
Sum ( $\Delta l = 1, \Delta s = 0$ ; $\Delta l = 0, \Delta s = 0$ )	Green and Stolarski [1972].
Ionization	Fite and Brackmann [1959].

determined by assuming that they are in quasi-equilibrium. The species with short lifetimes are:  $N_2(A^3\Sigma)$ ,  $N_2^+$ ,  $N^+$ ,  $O(^1D)$ ,  $O(^1S)$ ,  $O(^2D)$  and  $O_2(b^1\Sigma)$ . The seven species which have long lifetimes and are therefore integrated are:  $N(^4S)$ ,  $N(^2D)$ ,  $O^+$ ,  $NO^+$ ,  $O_2(a^1\Delta)$  and  $O_2^+$ .

Table 3.2 lists the chemical reactions and rates used in AURORA. Also in the code are important reactions with thermal electrons: dissociative recombination of  $N_2^+$ ,  $NO^+$ , and  $O_2^+$ , and electron impact deexcitation of the metastable states. Initial conditions for the constituents  $N_2$ ,  $O_2$ , and  $O$  can be taken from any of the desired standard models such as Jacchia 65 or 71 or Cira 65 tables. Initial conditions for the minor species are based on Strobel's [1971] calculations.

In addition to predicting atmospheric species densities as a function of altitude the code calculates both the volume emission and column emission of a variety of spectral lines in the UV, visible, and IR. AURORA presently monitors the 3914, 4278, and 4709 Angstrom emissions from the  $N_2^+(B\Sigma)$  state. These are a direct measure of the instantaneous deposition of auroral electrons. The McClatchey [1972] atmospheric absorption model for the visible and infrared lines is used to determine how much of the emission will survive the lower atmosphere.

To exercise the code, and to examine the buildup and decay of various ionization levels, the electron spectrum found in Figure 3.1 was used to obtain the results presented below. This spectrum is a slightly modified ICECAP spectrum (J. Ulwick, AFCRL, private communication) and corresponds in intensity to an ICB II aurora. The flux is isotropic downward (along the field) at 200 kilometers and the magnetic dip angle is  $77^\circ$ . In the results to follow, we have assumed this electron flux incident from time  $t = 0$  to  $t = 10$  seconds. Major atmospheric constituents were obtained from the

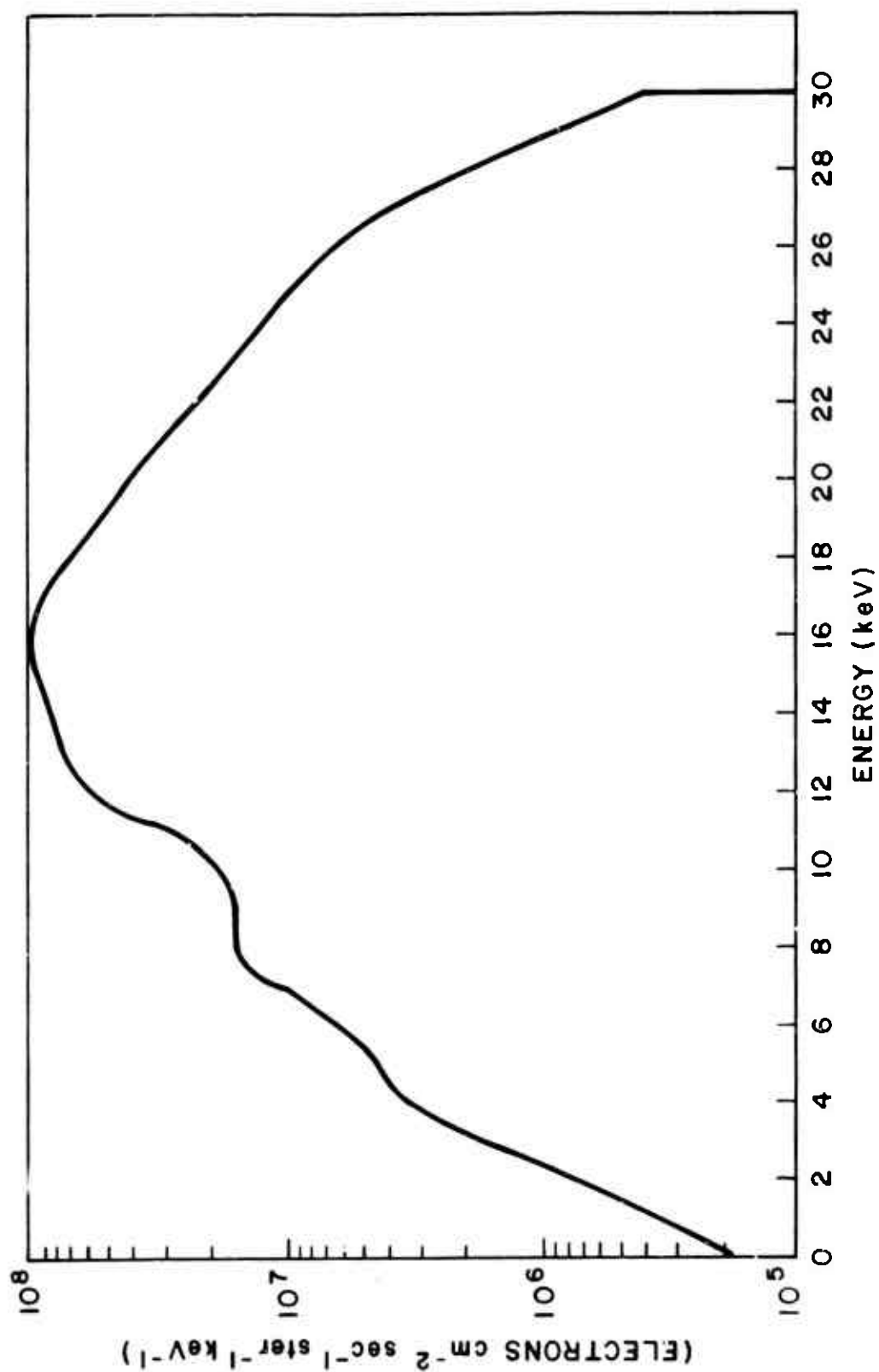


Fig. 3.1 — Assumed input electron spectrum used to exercise AURORA.  
This spectrum is a slightly modified ICECAP spectrum.

Table 3.2

## CHEMISTRY RATES IN AURORA (Temperature in ev)

Reaction	Rate	Reference
(1-C) $N^+ + O \rightarrow N + O^+$	$1.0 \times 10^{-12}$	Estimate
(2-C) $N^+ + NO \rightarrow N + NO^+$	$8.0 \times 10^{-10}$	Fehsenfeld [1972]
(3-C) $N^+ + O_2 \rightarrow N(^2D) + O_2^+$	$2.8 \times 10^{-10}$ $T_i < .4$ $4.8 \times 10^{-10}$ $T_i^{(.57)} > .4$	McFarland [1973]
(4-C) $O^+ + O_2 \rightarrow O + O_2^+$	$4.6 \times 10^{-12}$ $T_i^{-.4} < .155$ $1.0 \times 10^{-10}$ $T_i^{1.2} > .155$	McFarland [1973]
(5-C) $O^+(^2D) + N_2 \rightarrow O + N_2^+$	$7.0 \times 10^{-10}$	Rutherford [1971]
(6-C) $O^+(^2D) + O_2 \rightarrow O + O_2^+$	$3.0 \times 10^{-10}$	Stebbing [1966]
(7-C) $N_2^+ + O_2 \rightarrow N_2 + O_2^+$	$3.3 \times 10^{-10}$	Fehsenfeld [1972]
(8-C) $N_2^+ + O_2 \rightarrow N_2 + O_2^+$	$2.9 \times 10^{-12}$ $T_i^{-.8} < .3$ $3.9 \times 10^{-11}$ $T_i^{1.4} > .3$	McFarland [1973]
(9-C) $O_2^+ + N(^2D) \rightarrow O_2 + N^+$	$2.5 \times 10^{-10}$	Strobel [1974]
(10-C) $O_2^+ + NO \rightarrow O_2 + NO^+$	$6.3 \times 10^{-10}$	Fehsenfeld [1970]
(1-RN) $N + NO \rightarrow N_2 + O$	$2.7 \times 10^{-11}$	Garvin [1973]
(2-RN) $N + O_2 \rightarrow NO + O$	$1.3 \times 10^{-10}$ $T_n \exp(-.271/T_n)$	Garvin [1973]

Table 3.2 (Con't)

Reaction	Rate	Reference
(3-RN) $N + O_2(a^1\Sigma) \rightarrow NO + O$	$2.0 \times 10^{-14} \exp(-.052/T_n)$	Wayne [1970]
(4-RN) $N(^2D) + NO \rightarrow N_2 + 1/3$ $\cdot O + O(^1D) + O(^1S)$	$7.0 \times 10^{-11}$	Garvin [1973]
(5-RN) $N(^2D) + O_2 \rightarrow NO + O$	$4.4 \times 10^{-11} T_n^{1/2}$	R. R. Handbook [1972]
(1-RI) $N + O_2^+ \rightarrow NO^+ + O$	$1.8 \times 10^{-10}$	Fite [1969]
(2-RI) $N^+ + O_2 \rightarrow NO^+ + O$	$2.8 \times 10^{-10} T_i < .4$ $4.8 \times 10^{-10} T_i^{(.57)} T_i > .4$	McFarland [1973]
(3-RI) $O + N_2^+ \rightarrow NO^+ + N(^2D)$	$1.4 \times 10^{-10}$	Fehsenfeld [1970]
(4-RI) $O^+ + N_2 \rightarrow NO^+ + N$	$T_L = \text{MAX}(T_i, T_v)$ $3.1 \times 10^{-14}/T_L T_L < .065$ $1.2 \times 10^{-10}/T_L^2 T_L > .065$	McFarland [1973]
(1-Q) $N(^2D) + O \rightarrow N + O(^1D)$	$2.0 \times 10^{-13}$	Estimate
(2-Q) $O(^1D) + NO \rightarrow O + N_2$	$5.5 \times 10^{-11}$	Garvin [1973]
(3-Q) $O(^1D) + NO \rightarrow O + NC$	$2.1 \times 10^{-10}$	Garvin [1973]
(4-Q) $O(^1D) + O_2 \rightarrow 1/4 O_2$ $+ 3O_2(b^1\Sigma) + O$	$7.5 \times 10^{-11}$	Garvin [1973]
(5-Q) $O(^1S) + O \rightarrow O(^1D)$ $+ O(^1D)$	$7.5 \times 10^{-12}$	Garvin [1973]

Table 3.2 (Con't)

Reaction	Rate	Reference
(6-Q) $O(^1S) + NO \rightarrow O + NO$	$3.4 \times 10^{-9} T_n^{1/2}$	Garvin [1973]
(7-Q) $O(^1S) + NO \rightarrow O + NO$	$4.3 \times 10^{-12} \exp(-.073 \cdot T_n)$	Garvin [1973]
(8-Q) $N_2(A^3\Sigma) + N \rightarrow N_2 + N$	$5.0 \times 10^{-11}$	Young [1968]
(9-Q) $N_2(A^3\Sigma) + O \rightarrow N_2 + O$	$1.0 \times 10^{-10}$	Shemansky [1971]
(10-Q) $N_2(A^3\Sigma) + O \rightarrow N_2 + O(^1S)$	$5.0 \times 10^{-12}$	
(11-Q) $N_2(A^3\Sigma) + NO \rightarrow N_2 + NO$	$2.6 \times 10^{-10}$	Shemansky [1971]
(12-Q) $N_2(A^3\Sigma) + O_2 \rightarrow N_2 + O_2$	$9.0 \times 10^{-12}$	Shemansky [1971]
(13-Q) $O_2(a^1\Delta) + O \rightarrow O_2 + O$	$1.0 \times 10^{-17}$	Clark [1969]
(14-Q) $C_2(a^1\Delta) + O_2 \rightarrow O_2 + O_2$	$4.1 \times 10^{-17} T_n^{(.8)}$	Garvin [1973]
(15-Q) $O_2(b^1\Sigma) + N_2 \rightarrow C_2 + N_2$	$2.0 \times 10^{-15}$	Zipf [1969]
(16-Q) $O_2(b^1\Sigma) + O_2 \rightarrow O_2 + O_2$	$1.5 \times 10^{-16}$	Garvin [1973]

CIRA 1965 model 5 hour 0. Temperatures were assumed to be the ambient neutral values given in this CIRA model. To examine the effect of elevated temperatures we also present the results of a "hot ion" model in which, instead of ambient temperatures, we assumed the ion temperatures to be 1 eV and the electron temperatures to be 0.1 eV. Figures 3.2 and 3.3 show the species concentrations of  $O^+(^4S)$ ,  $O^+(^2D)$ , and  $NO^+$ . The ratio of  $NO^+$  to  $O^+$  is shown in Figure 3.4.  $O^+(^2D)$  charge exchanges very rapidly with  $N_2$  and  $O_2$  so that it disappears as soon as the auroral flux is turned off. The  $O^+(^2D)$  profile will be unchanged with time for a constant input flux because it equilibrates almost instantaneously and because its production and destruction rates are dependent on O and on  $N_2$  and  $O_2$  respectively. These species maintain their ambient values.

The production of  $NO^+$  is due primarily to the  $N_2^+$ , O rearrangement reaction and  $O_2^+$ , NO charge exchange.  $NO^+$  is destroyed only by dissociative recombination. Since  $O_2^+$  and  $N_2^+$  disappear rapidly when the flux is turned off, so does  $NO^+$  production. Because  $NO^+$  is the terminal ion, its production rate is directly proportional to the incident flux. In Figure 3.4, the ratio  $NO^+/O_2^+$  rises steadily after the source is turned off. This is a manifestation of the fact that  $NO^+$  is the terminal ion and disappears more slowly, i.e., the  $NO^+$  recombination time exceeds the  $O_2^+$  charge exchange time constant. To examine other species and levels and to consider the effect of long-term energy deposition (to  $10^4$  seconds), the reader is referred to Hyman and Julienne [1974].

The results presented here agree well with the number densities and chemical species typically measured in IBC II auroras. It is necessary now to obtain measured electron fluxes and species emissions to compare experimental values with results predicted by AURORA. Such an effort is currently underway and the results



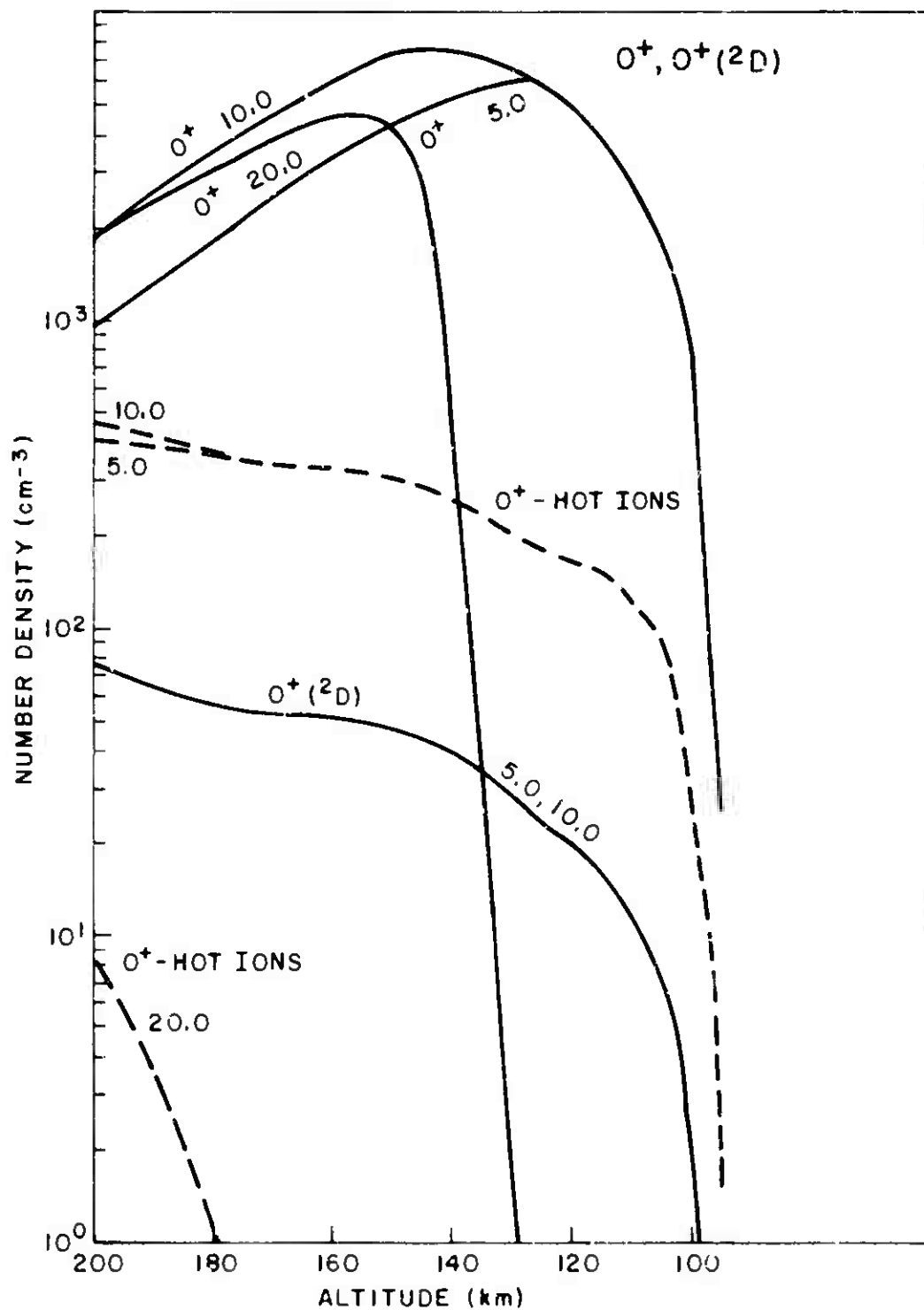


Fig. 3.2 —  $\text{O}^+$  ( $^1\text{S}$ ) and  $\text{O}^+$  ( $^2\text{D}$ ) profiles 5.0, 10.0 and 20.0 seconds after electron flux is turned on. Flux is turned off at 10.0 seconds.

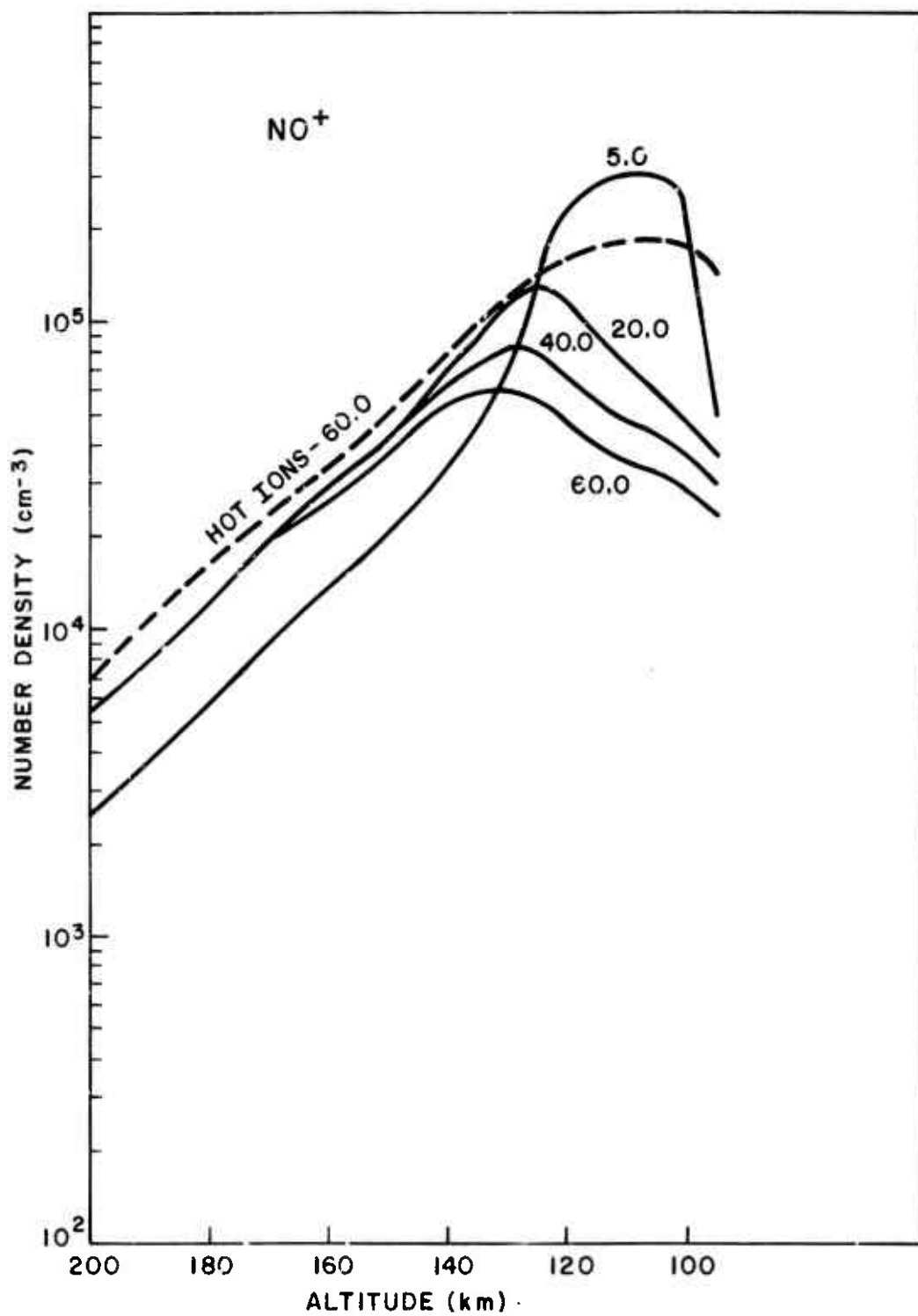


Fig. 3.3 — NO<sup>+</sup> profiles 5.0, 20.0, 40.0, and 60.0 seconds after electron flux is turned on. Flux is turned off at 10.0 seconds.

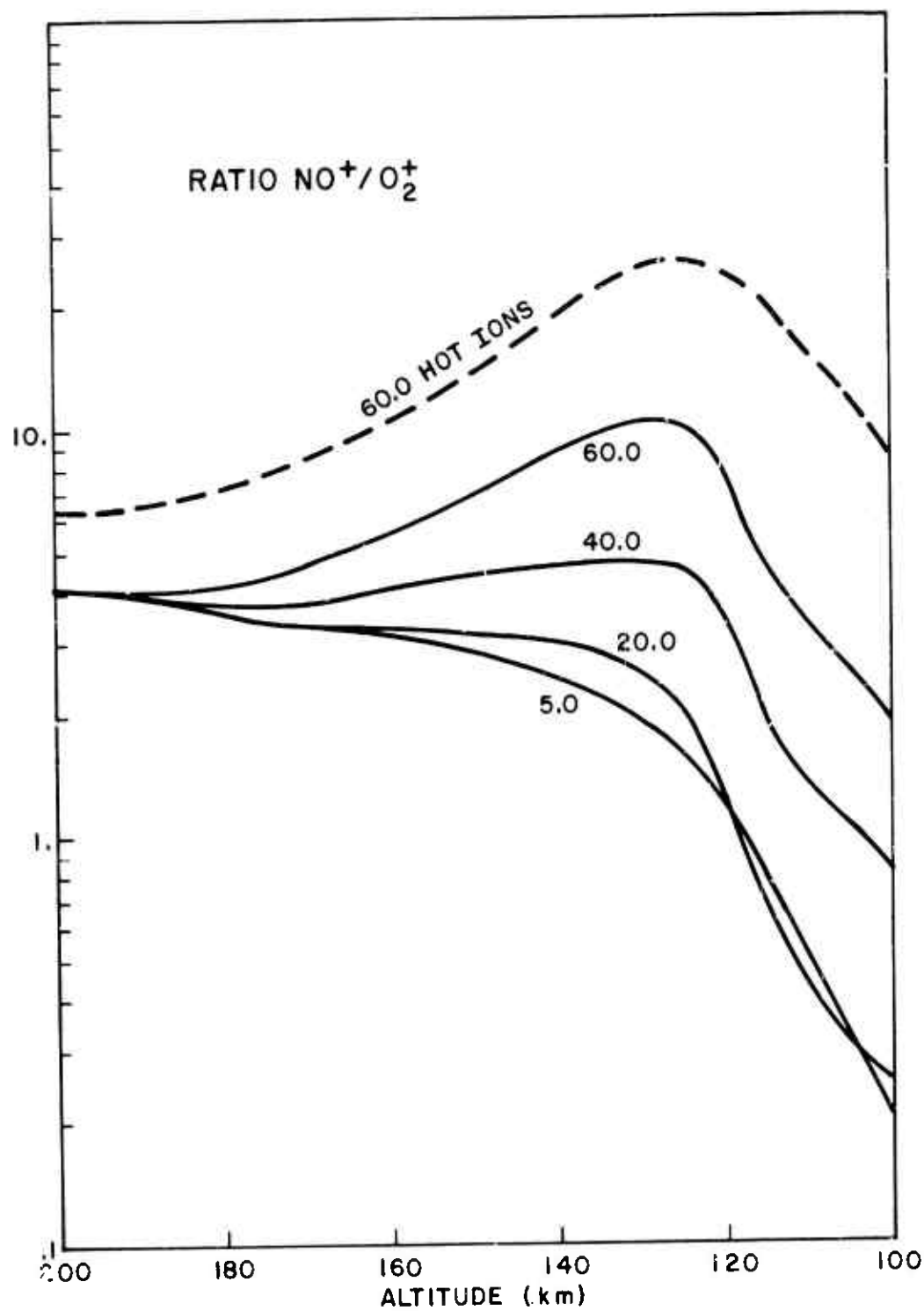


Fig. 3.4 — Profiles of ratio of  $\text{NO}^+$  to  $\text{O}_2^+$  5.0, 20.0, 40.0, and 60.0 seconds after electron flux is turned on. Flux is turned off at 10.0 seconds.

of this study should be reported early next year. Zipf's [1969] observations of aurora with very high NO densities (greater than  $10^{10} \text{ cm}^{-3}$ ) and very large  $\text{NO}^+/\text{O}_2^+$  ratios have provoked extreme interest in examining the efficiency of converting the energy of precipitating electrons to the formation of the NO molecules. In preliminary calculations we have been able, by making various speculative assumptions, such as increased ion temperatures, to duplicate the emissions observed by Zipf. Future work will continue these calculations and will couple predictions from AURORA with the auroral arc modeling reported in the next section to examine the effects of Joule heating and transport of species resulting from electric fields and currents.

## Section 4

### AURORA ARC MODELING

J.A. Fedder and J.H. Orens

In developing an ionospheric model to predict the current, electric fields, and plasma densities in auroral arcs, we are working in an area which has almost direct applicability to HANE phenomenology. Note that we are not concerned here with the high beta flows that are best handled by the MHD HANE codes (MICE and MRHYDE), but with the lower beta flows characteristic of the weakly ionized part of the UV fireball, of the late-time motion of the nuclear disturbed ionosphere, and the auroral plasma. The correlations are apparent, e.g., the space and time scales are similar (tens to thousands of kilometers and minutes to hours), the boundary conditions are essentially the same, the electron densities are similar ( $10^4 \text{ cm}^{-3}$  to  $10^7 \text{ cm}^{-3}$ ), and the magnetic field is constant (low beta).

The auroral arc modeling program at NRL started with the development of a simple two-dimensional model. The results of calculations made with the model were shown to be in qualitative agreement with certain measurements of auroral currents and electric fields. This model was then dimensionally extended and applied to the examination of the convection of the ionospheric plasma in the midnight region of the auroral oval. Once again, the results obtained with this model were shown to be in good qualitative agreement with patterns inferred from measurements. Both modeling efforts are described below.

#### 4.1 THE 2-D AURORAL ARC MODEL

The simple, two-dimensional auroral arc model developed the past year (see Fedder [1974]) was initiated to calculate auroral arc

currents, electric fields, and plasma densities in the ionosphere. The are model is based on two assumptions:

- Currents in the ionosphere and in the auroral are are determined by the conductivity and the ionospheric electric field. Owing to the inhomogeneous plasma density and electric field gradients. Birkeland currents flow parallel to the geomagnetic field. The closure of the Birkeland currents in the magnetosphere is not specified.
- The ionospheric electric field is the superposition of the magnetospheric convection electric field and a magnetic field-aligned potential created by the existence of the Birkeland currents and a field-aligned resistivity.

The are model is constructed in a Cartesian system with the z-axis positive upward, the x-axis normal to the auroral are, and the y-axis parallel to the are. The geomagnetic field is along the z-axis, and the imposed uniform magnetospheric electric field is either normal or parallel to the are. Assuming that the vertical motion of ions is unimportant, that the difference in number density between ions and electrons is negligible, and that the auroral arc and ambient ionosphere are created by an assumed ionization production rate,  $P(x, z)$ , the are model is defined by the following set of equations:

$$\frac{\partial n}{\partial t} = \frac{\partial}{\partial x} n v_x + P(x, z) - \alpha n^2, \quad (4.1)$$

$$v_x = \mu_p \frac{c E_x}{B} - \mu_h \frac{e E_y}{B}, \quad (4.2)$$

$$\frac{\partial}{\partial z} j_{\parallel} = - \frac{\partial}{\partial x} j_x, \quad (4.3)$$

$$E_x = E_{x_0} - \frac{\partial}{\partial x} J_{\parallel} (x) R(x) L \quad (4.4)$$

$$E_y = E_{y_0}, \text{ and}$$

$$J_{\parallel}(x) = \int_{z_0}^{z_t} \frac{\partial j_{\parallel}(x, z)}{\partial z} dz, \quad (4.5)$$

where  $n$  = ion density

$v_x$  = x-component of ion velocity

$\alpha$  = recombination rate

$\mu_p, \mu_n$  = Pederson and Hall mobilities

$E_x, E_y$  = ionospheric electric fields in x and y directions

$j_{\parallel}$  = field-aligned Birkeland current carried by electrons

$j_x$  = ionospheric current in the x-direction

$R(x)$  = field aligned resistivity

$L$  = length of resistive region

$J_{\parallel}(x)$  = Birkeland current density at top of ionosphere, and

$z_0, z_t$  = lower and upper ionospheric boundaries.

$B$  = geomagnetic field strength

$c$  = speed of light.

These equations form a complete set describing an auroral arc in the ionosphere. They can be solved explicitly in time to arrive at a steady-state solution. Appropriate descriptions of  $P(x, z)$ ,  $\alpha$ ,  $R(x)$ ,  $L$ , and  $E_{x_0}$  and  $E_{y_0}$  must be supplied.

There are two questionable assumptions inherent in the above equations: first, that the ionospheric electric field does not vary with height; and second that the ions do not move vertically. For this preliminary effort, these assumptions were justified solely on the grounds that they simplified the numerical calculations. As this work is continuing, these assumptions are being removed.

To examine this model and make qualitative comparisons with measurements, we will assume that the ionization production rate consists of an ambient ionization rate, and an arc ionization rate.

$$P(x, z) = P_{\text{amb}}(z) + P_{\text{arc}}(x, z)$$

We assume:

$$P_{\text{amb}}(z) = 30\% \text{ cm}^{-3} \text{ sec}^{-1}, \text{ and}$$

$$P_{\text{arc}} = 7.5 \times 10^4 \exp[-0.004 (x - x_A)^2] \\ \times \begin{cases} Az^2 + Bz + C; & z \leq 120 \text{ km} \\ \exp[0.025 (120 - z)]; & z \geq 120 \text{ km} \end{cases}$$

where  $x$  and  $z$  are in km, and the arc is centered at  $x_A$ .  $A$ ,  $B$ , and  $C$  are chosen so that

$$Az^2 + Bz + C = 1 \quad \text{at } z = 120$$

$$Az^2 + Bz + C = 0 \quad \text{at } z = 100$$

$$2Az + B = 0 \quad \text{at } z = 115$$

The arc ionization profile approximates the results of Romick and Belon [1967, Figure 13], and the ambient profile is a simple approximation based only on expected levels and trends.

Specifying a constant ionospheric convection velocity, we can examine and review the applicability of the model in more detail. Assuming  $E_{x_0} = 25 \text{ m V m}^{-1}$ ,  $E_{y_0} = 0$ , and a stationary auroral arc source,



will generate the results shown in Figures 4.1 and 4.2. This model should be applicable to east-west aligned arcs in the evening sector of the auroral oval with the electric field and x-axis directed northward. It should also be applicable to east-west aligned arcs in the morning sector, but with the electric field and x-axis directed southward.

The Birkeland currents plotted in Figure 4.1 form oppositely directed sheet currents on either side of the arc. They close the ion Pederson current which flows through the arc in the direction of increasing x. The ionospheric electric field is greater than the magnetospheric field on the edge of the arc, but is 50 percent less in the center of the arc. The "M" shaped field in the vicinity of the arc is characteristic of all computations to date.

Figure 4.2 shows computed plasma and current density profiles. Note the distortion of the plasma contours at altitudes where the Pederson currents occur. In the absence of an electric field, these contours would be tear-drop shaped. The y-directed ionospheric currents form an arc-associated electrojet which is broadened by the enhanced field at the arc edges.

In a recent article, Maynard et al.[1973] discusses the data for electric fields in precipitation regions. Allowing for a number of contrary results, they conclude that the electric field magnitude and particle precipitation are anticorrelated. This is in agreement with the above results, and in fact it is expected that more measurements would agree with these results. This is because arcs are generally observed to be aligned in an east-west direction around the auroral oval.

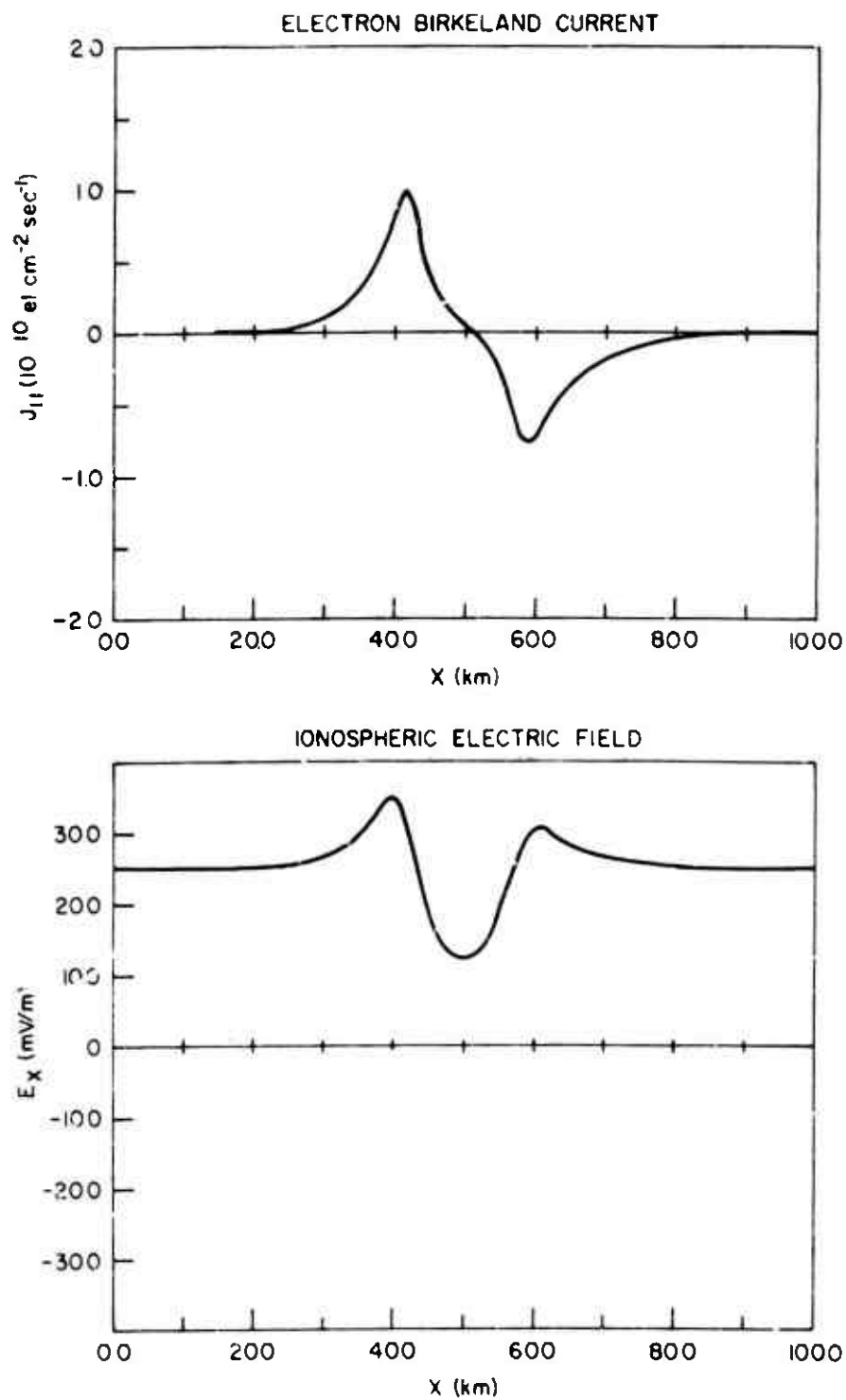


Fig. 4.1 — Calculated auroral electron Birkeland currents and ionospheric electric field normal to an arc

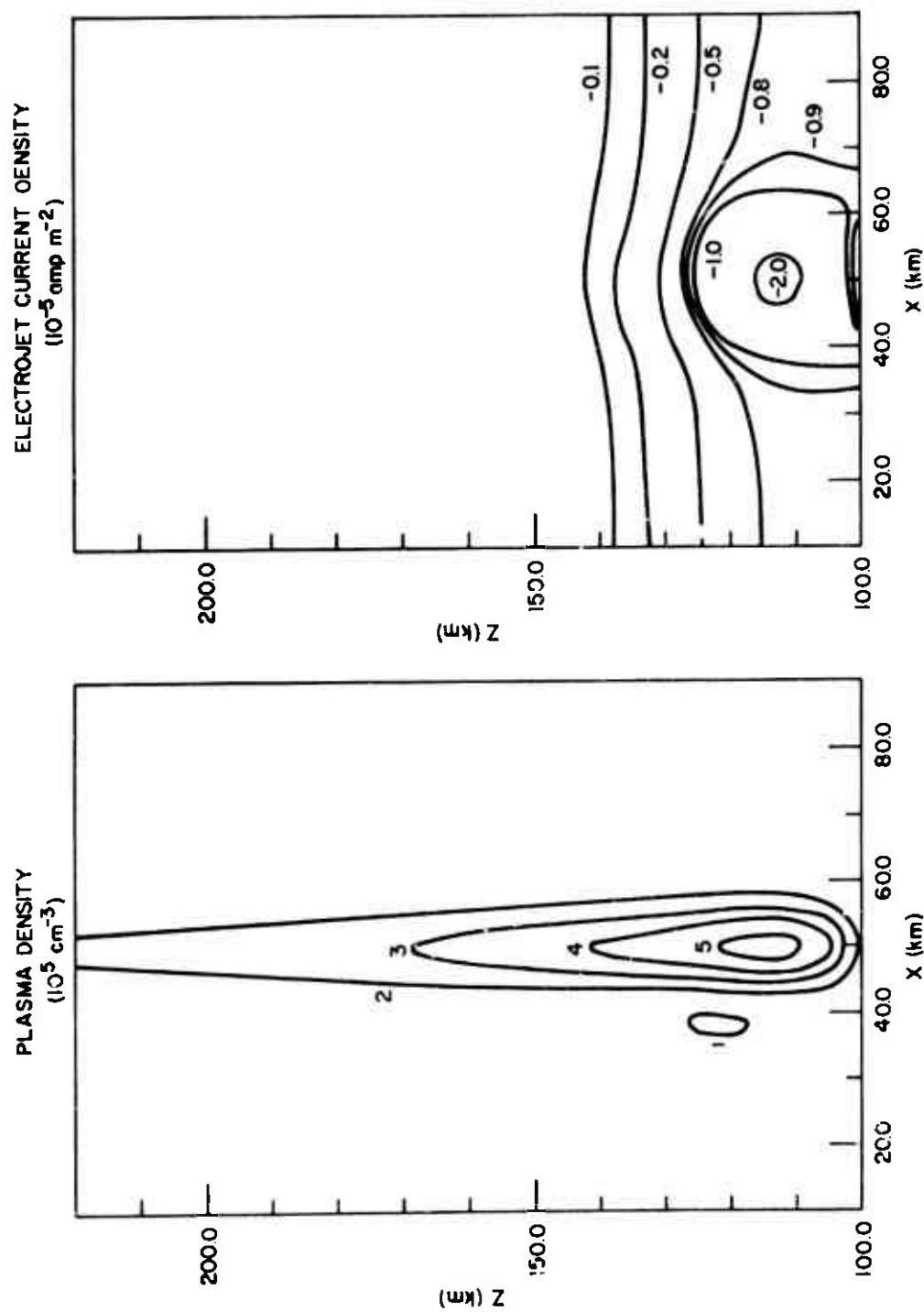


Fig. 4.2 — Calculated auroral arc plasma density and associated electrojet

The results for currents computed with this model also agree qualitatively with measurements of arc currents. In particular, the example above shows an eastward electrojet and the Birkeland current out of the ionosphere to the north of the current in agreement with Cloutier [1973]. The fact that the current density distribution does not agree with that which has been measured is not a serious fault of the model. The distribution is a sensitive function of the assumed form of the magnetospheric convection field and of the anomalous resistance which are both unknown for the current measurements. In future work we will show how changes in the assumed form of the field aligned resistance can result in different Birkeland current distributions.

#### 4.2 EXTENDED AURORAL ARC MODELING

As a next step in improving both modeling capability and our understanding of the auroral process, a numerical simulation of the convection of ionospheric plasma in the midnight region of the auroral oval was performed. To explain the general features of the polar region ionospheric currents which lead to magnetic disturbances, Axford and Hines [1961] introduced the idea of a magnetospheric convection. There have been numerous other papers since then about the nature and causes of magnetospheric convection, a large number of which calculate plasma convective flow patterns in the magnetosphere and ionosphere using relatively simple models. Although these models show some agreement with data, they are not completely convincing. This is primarily because they are either essentially one-dimensional calculations or the assumptions on which they are founded are questionable. Our extension of some of these ideas into multiple dimensions has resulted in excellent agreement with data.

In performing this simulation, the ionospheric plasma continuity equation, the ionospheric current continuity equation, and an equation for the ionospheric electric potential must all be solved simultaneously. The calculations are performed in a three-dimensional right-hand Cartesian grid centered at midnight ( $x = 0$ ,  $y = 0$ ). The  $x$ -axis is directed southward, the  $y$  eastward, and the calculations cover an area 1500 km square in  $x$  and  $y$  and 105 km high ( $95 \leq x \leq 200$  km). The simulation requires assumed ionospheric plasma production and recombination rates, the magnetospheric convection electric potential, and a resistance to the field aligned Birkeland current. The mathematical formulation extends the previously described auroral arc equations into a third dimension.

The ion continuity equation in the auroral ionospheric E-region is defined as

$$\frac{\partial n}{\partial t} = - \frac{\partial}{\partial x} n v_x - \frac{\partial}{\partial y} n v_y + P - \alpha n^2$$

where

$n$  = ion density

$P$  = ion production rate

$\alpha$  = volume recombination rate, and

$v_x$ ,  $v_y$ , the ion velocities, are defined as

$$v_x = \mu_p \frac{c E_x}{B} - \mu_h \frac{c E_y}{B} ,$$

$$v_y = \mu_p \frac{c E_y}{B} + \mu_h \frac{c E_x}{B}$$

where

$\mu_p, \mu_h$  = Pedersen and Hall mobilities

$c$  = speed of light

$B$  = geomagnetic field strength (=0.5 Gauss), and

$E_x, E_y$  = x and y components of ionospheric convection electric field.

Diffusive transport and vertical transport of ionization have been neglected since it is expected that horizontal convective transport dominates.

The ionospheric current continuity equation is

$$\frac{\partial}{\partial z} j_{\parallel} = - \frac{\partial}{\partial x} j_x - \frac{\partial}{\partial y} j_y$$

where

$j_{\parallel}$  = Birkeland current density (assumed carried by electrons)

$j_x, j_y$  = horizontal ionospheric currents  
 $qn(v_x - v_x^e), qn(v_y - v_y^e)$

where

$q$  = electron unit charge, and

$v_x^e, v_y^e$  = electron velocities  
 $\frac{-c E_y}{B}, \frac{c E_x}{B}$

For the electric field,

$$\underline{E} = - \nabla \psi$$

$$\psi = \psi_m + J_{\parallel} R$$

where

$\psi$  = ionosphere electric potential,

$\psi_m$  = assumed magnetosphere potential,

$J_{\parallel}$  = total Birkeland current entering and leaving ionosphere, and

$R$  = assumed anomalous resistance to  $J_{\parallel}$ .

Figure 4.3 shows the assumed magnetospheric convection pattern as it maps along field lines onto the ionosphere. The resulting electric field in the polar cap ionosphere is 25 mV m westward at midnight.

The ionospheric convection pattern is shown in Figure 4.4. It is considerably different from the magnetospheric pattern shown in Figure 4.3. The difference is caused by a field aligned potential between the magnetosphere and ionosphere. The most important feature of the pattern is the westward shift of the east-west convective discontinuity before midnight. This behavior has been reported by a number of experimenters. In particular, one should note the similarity between the calculated pattern and the pattern inferred from measurements by Heppner [1972].

The southward electric field along three north-south planes through the auroral oval is shown in Figure 4.5. The changing field direction is very similar to a measurement of Gurnett and Frank [1973]. The Birkeland current density patterns are presented in Figure 4.6. The pattern seen here is the same as that observed in the measurements of Armstrong and Zmuda [1974]. The very large amplitude of the current out of the ionosphere at the northern border west of midnight is largely responsible for closing the eastward and westward electrojets.

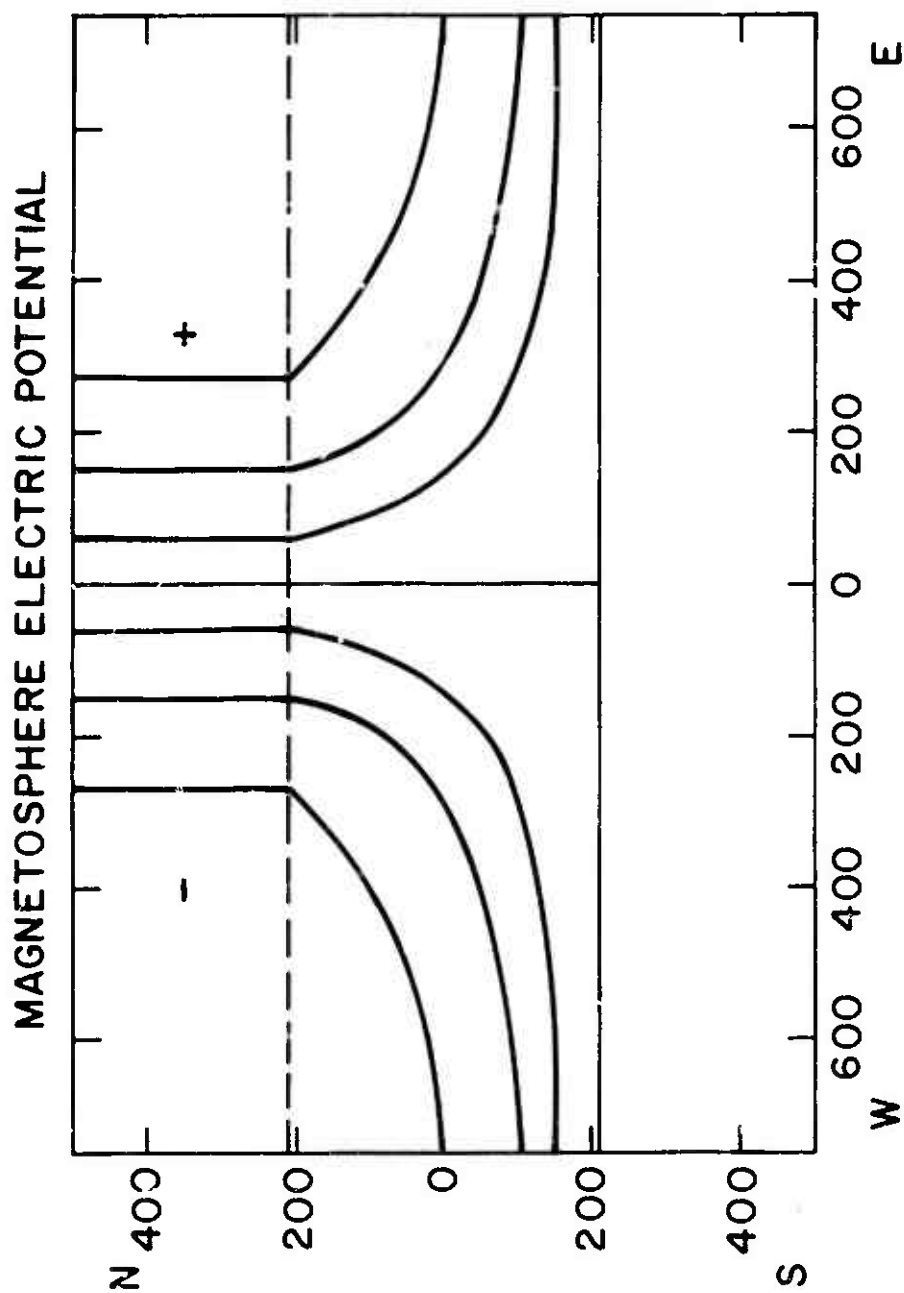


Fig. 4.3 — This figure shows the model auroral oval geometry and the magnetosphere convection pattern mapped on the ionosphere. The dashed line across the upper part of the figure and the solid line across the lower part are the poleward and equatorward boundaries of the oval, respectively.



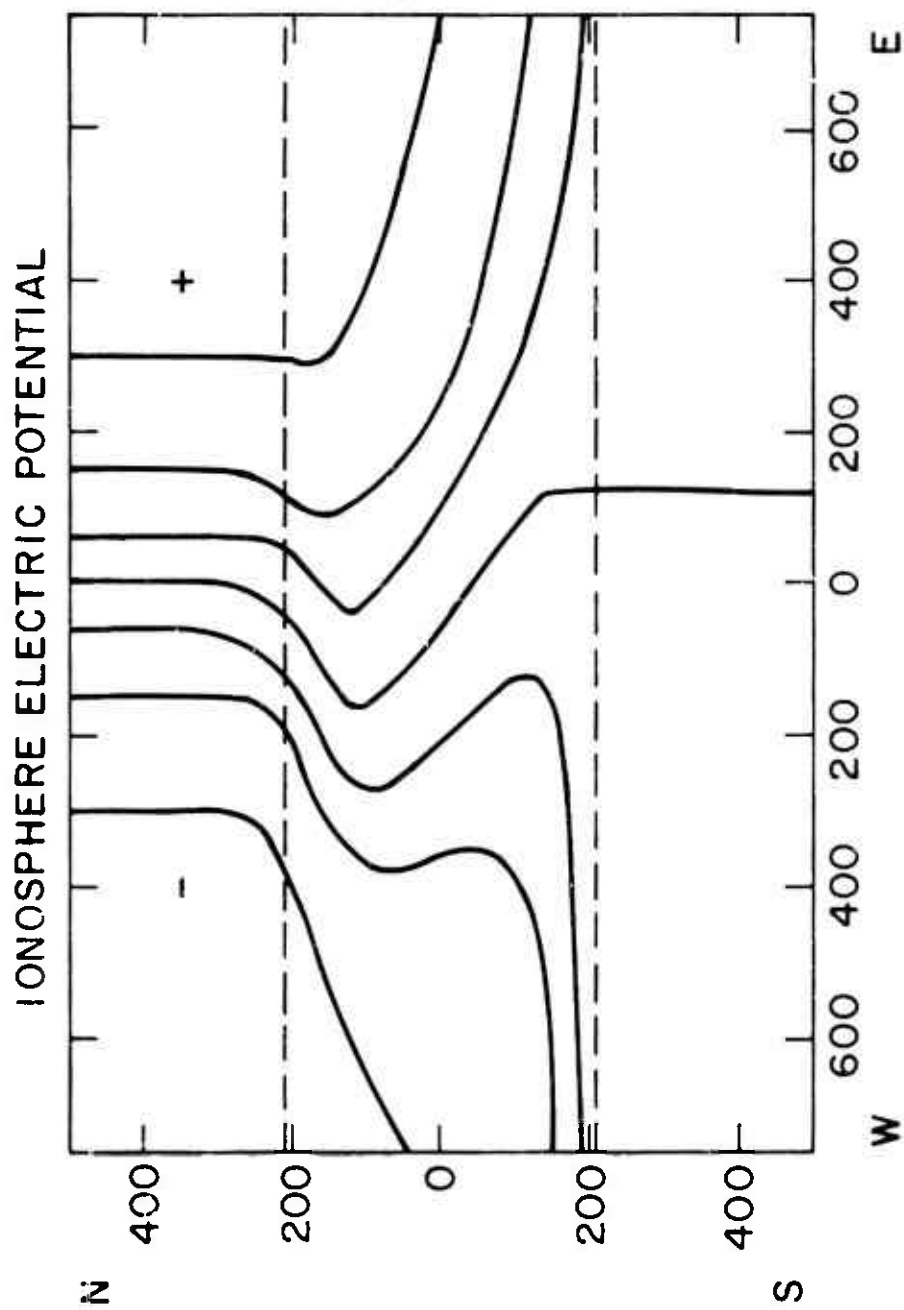


Fig. 4.4 — The ionospheric convection pattern which results from polarization of the auroral oval and the field-aligned potential drops. Note the multiple reversals to the west of midnight.

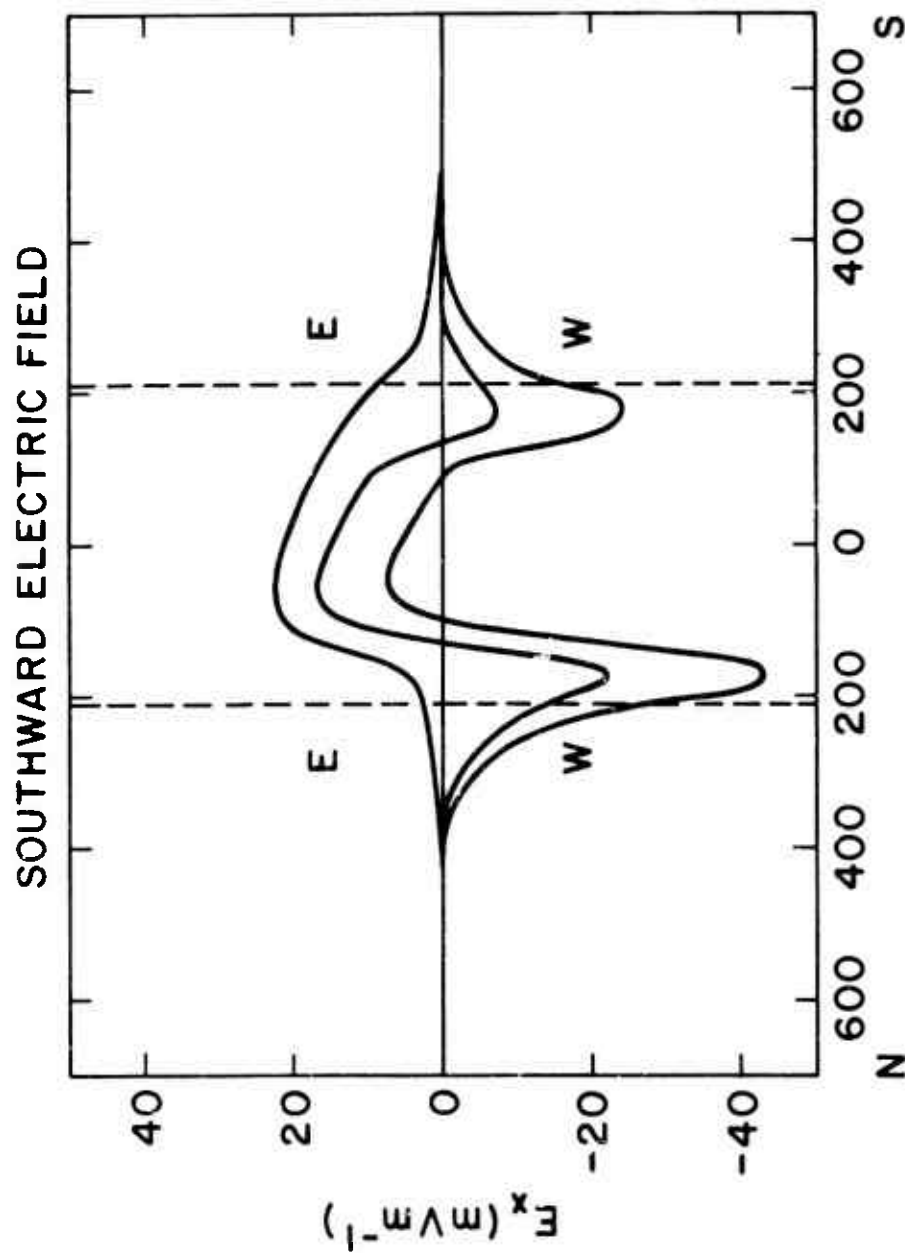


Fig. 4.5 — The north-south electric field associated with Fig. 4.4 on three north-south planes through the oval. The top curve is at a location 300 km east of midnight; the middle curve, at midnight; and the lower curve, 300 km west of midnight.

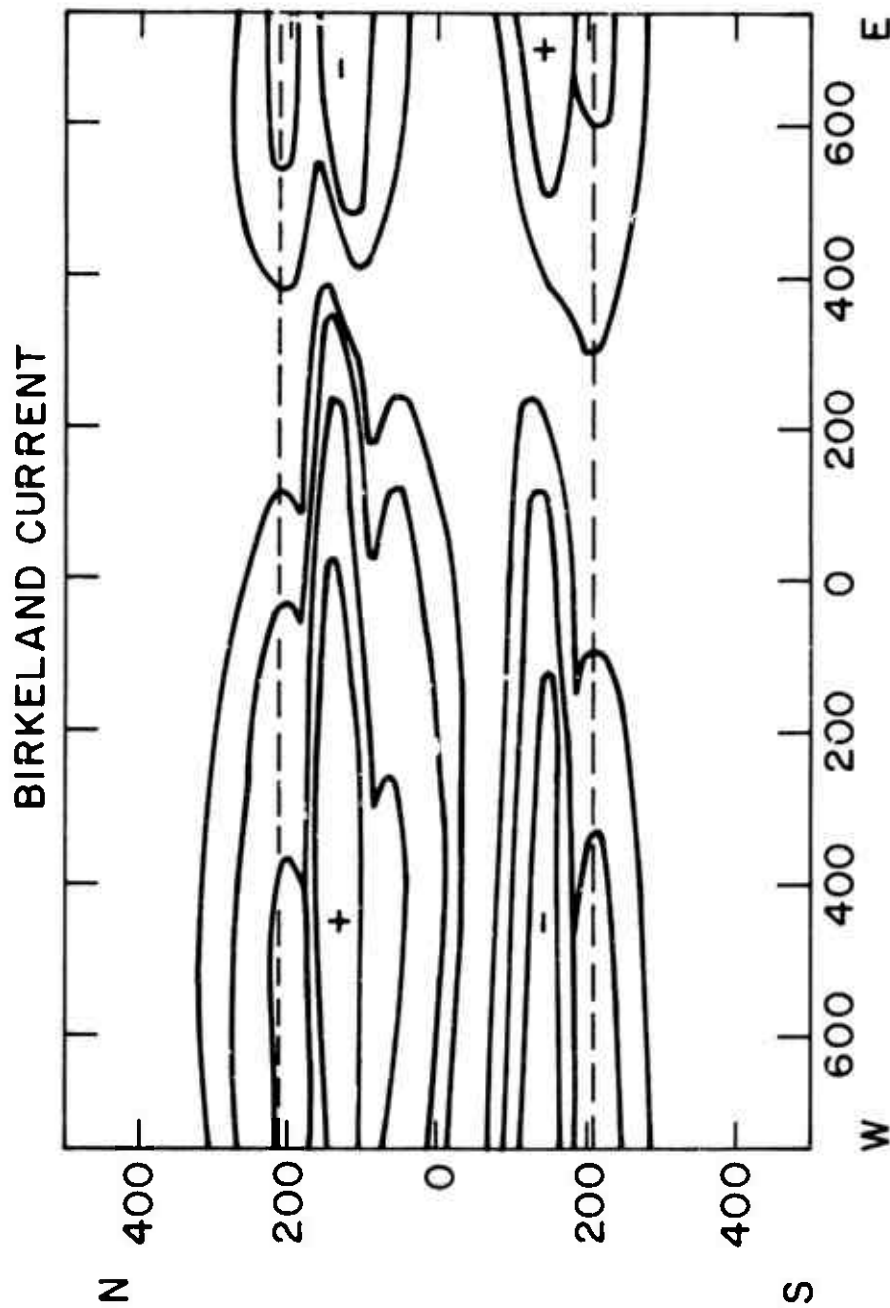


Fig. 4.6 — Birkeland current system in midnight auroral oval. Plus signs signify current out of and minus signs, current into the ionosphere. The current density in the central contour of the northern evening sheet is  $3 \times 10^9$  el.  $\text{cm}^{-2} \text{ sec}^{-1}$ ; each succeeding outward contour is reduced by a factor of 2.

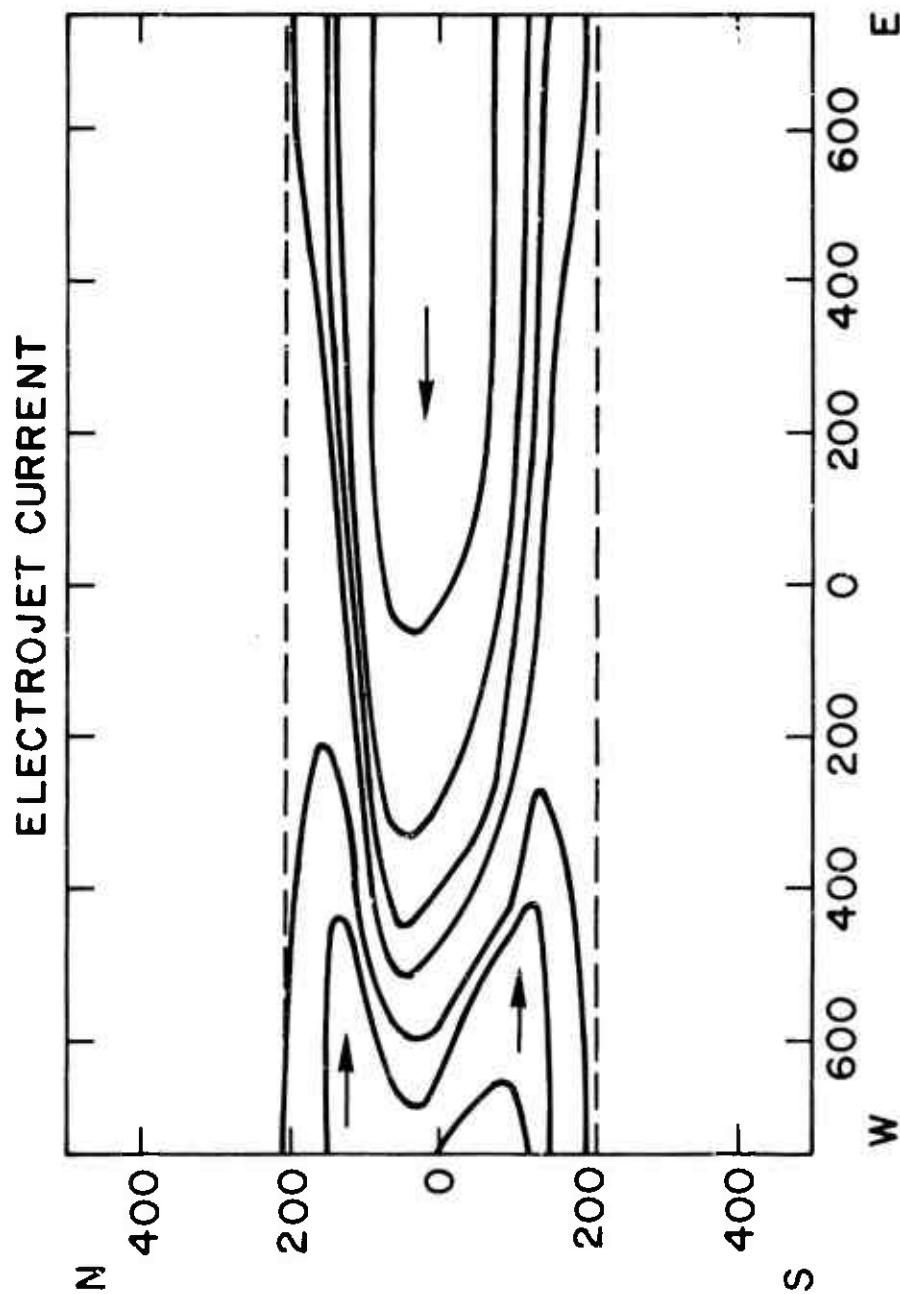


Fig. 4.7 — The electrojet system in the midnight sector of the auroral oval showing both the eastward and westward jets (arrows show direction). The central contour in the westward electrojet is  $133 \text{ amp km}^{-1}$  height integrated current density. Consecutive contours outward are each reduced a factor of 2.

Figure 4.7 is a contour map of the auroral electrojet current. The most important feature here is the extension, some 500 km to the west of midnight, of the westward electrojet. This is a feature of the westward jet that has been recognized from geomagnetic observations by Harang [1946] and Heppner [1972]. The overlap of the eastward and westward electrojets in the southern part of the oval has also been observed in geomagnetic data.

Based upon the results generated with the above model, we may make some tentative conclusions concerning certain features of the auroral oval. The Birkeland current systems appear to close a sizable portion of the intense currents in the midnight oval. This includes not only the north-south Pedersen currents, but also the eastward and westward electrojets. The Birkeland currents occur in sheet-like structures at the northern and southern edges of the oval for two reasons; first because of the imposed magnetospheric electric field pattern, and second because of the essentially east-west alignment of the auroral plasma density enhancement.

With satellite photography of the aurora [Snyder et al., 1974], it has become clear that the aurora occurs in two forms; diffuse aurora and discrete aurora [Akasofu, 1974]. Comparing the patterns of these two forms with the Birkeland current patterns shown above, indicates that the discrete aurora occurs primarily in the region of large amplitude upward Birkeland currents and field aligned potential, while diffuse aurora appear to occur in regions where the field-aligned potential either opposes electron precipitation or is weak.

## Section 5

### SUMMARY AND CONCLUSIONS

In the introduction, we briefly discussed the rationale for initiating efforts to numerically simulate auroral processes. The impulsive, transient disturbances of the ionosphere and atmosphere found in an aurora are not as great as those found near a HANE, but are similar to those reached in the wings of a UV fireball, in a beta batch, or at late times in atmospheric heave. Many of the mathematical relationships necessary to the simulation of HANE phenomenology are also used in simulating auroral processes. More importantly, many of these relationships are not amenable to direct analytic solution and must therefore be solved numerically.

Since we are unable to conduct HANE tests, and because much of the data acquired during previous HANE tests are not applicable to the technical questions raised today, we must rely heavily on our ability to simulate HANE phenomenology in the paper exercise of certain defensive systems and strategies. Confidence in the results of these exercises can best be established when as much of the overall simulation model as possible has been exercised to reproduce appropriate natural or man-made atmospheric disturbances. The largest available natural disturbance against which the simulation model can be checked, one which will regularly occur for repeated checks and investigation, is the aurora.

In developing an auroral model, there are three technical areas which must be addressed: first is the deposition of energy into the upper atmosphere by energetic electrons and protons, second is the complex series of chemical reactions initiated by this energy deposition, and third is the perturbation or creation of fields and

currents in the ionosphere. All three areas have direct applicability to HANE modeling; however, proper scaling relationships or modifications must be used. Each of these areas has been addressed by the Plasma Dynamics Branch during the past year and significant progress has been made in understanding both auroral and HANE phenomenology.

During the past year we have developed simplified fast running codes to model electron and proton energy deposition in the atmosphere. Both codes use a continuous slowing down approximation for the energy loss and handle cross-field energy diffusion in a minimal fashion. They therefore tend to underestimate energy deposition at higher altitudes and to overestimate atmospheric penetration. The codes are extremely useful however for making qualitative comparisons between calculated energy deposition, ionization rates, and optical emissions for different input spectra and conditions.

Electron energy deposition has also been modeled in more detail using a transport formulation which attempts to account for discrete energy losses and for large angle scattering, and which allows many angles to be included in specifying the input flux. A one-constituent  $N_2$  atmosphere is currently assumed, but O and  $O_2$  are now being added.

Early results from his detailed model were presented at a June 1974 DNA meeting. At that time results from this deposition code were shown to predict higher backscatter, shallower penetration, and higher deposition at high altitudes, than either the MRC or LMSC codes (its behavior relative to the CSD approach is as expected--see Figure 2.2). The model was further validated by confining scattering events to small angles to approximate the Fokker-Planck solutions and reproduce the reported LMSC energy deposition profile.

Energy deposition studies will continue in several areas over the next year. The transport code will be exercised to develop a better understanding of electron energy loss processes, and in particular of the magnitude of predicted backscatter. The high backscatter predicted by this code is a result of the basically different way in which the energy loss process is modeled and it is therefore necessary to obtain a detailed understanding of the role which this interaction plays in the energy loss process. This same code will be applied to the Starfish detonation in an attempt to model the observed emissions from the "hot" electron patch. The proton energy deposition work will be continued to model selected PCA event data, to handle the energy loss process in a more realistic manner and to extend the model to heavier particles such as debris ions.

The auroral chemistry code developed during the past year will accept energy deposition rates from the above models and follow the many reaction processes initiated by such a deposition to predict the ionization levels, and emission rates initiated. The deposition rates from the above codes can be scaled to simulate aurora of varying strengths for any selected input spectrum. The transient response of the atmosphere may be observed by turning the deposition rates on and off.

The processes incorporated have been described previously, but the more important ones included were:

- Dissociation of  $N_2$  as a source of  $N(^2D)$  which, reacting with  $O_2$ , is the dominant source of NO.
- The decay of certain highly excited states of  $N_2$  to supply a strong UV source. This UV ionizes  $O_2$  and  $^2O$  and dissociates  $O_2$ .



- Thermal electron reactions such as dissociative recombination of  $N_2^+$ ,  $NO^+$ , and  $O_2^+$  and electron impact deexcitation of metastable states.

Using a scaled ICECAP spectrum obtained from AFCRL measurements, the code has been exercised to demonstrate the predictions obtainable. The qualitative features of the predictions were as expected. They are now being validated quantitatively.

One phase of this validation will test both the electron deposition code and the auroral chemistry code. Measurements were made during ICECAP 72 of primary electron flux, electron-ion densities, positive ion densities, positive ion concentrations, and various emission rates for an IBC 11 aurora. The data was acquired with an instrumented Black Brant rocket, on both ascent and descent, that apparently passed just under the lower edge of the observed arc. By using measured electron fluxes in the deposition code and then generating emission rates with the auroral chemistry code, we should be able to reproduce the ICECAP field measurements.

Modeling the gross morphology of auroral arcs, and extending this work to the midnight auroral oval, has given us confidence that we can calculate large scale polarization and plasma density in arcs and in large ionospheric plasmas. The current systems generated in these models can be used to study the stability of auroral arcs to perturbations such as gradient drift waves. This capability is also necessary to provide background conditions for the striation and scintillation work described in Volume IV.

Currently, both the auroral arc model and the extension to the midnight oval are steady state calculations (in the sense that the driving functions are constant). During the next year this modeling will be extended to include time dependence. With this improvement in the model, transient fields and currents can be

followed, and the auroral response to impulsive inputs can be examined. Also during the next year, the arc model will be coupled with the auroral chemistry code to predict emission rates and ionization levels which are both influenced by auroral currents.

The simulations performed to date with the auroral modeling codes all have been qualitatively verified against a number of observations and measurements. This bolsters our confidence in these models and in our ability to extend the techniques to HANE phenomenology. A more detailed quantitative check of these same codes is necessary as is more predictive work on expected emission rates, communications disruptions, etc.

The ongoing HAES program, with experimental efforts such as ICECAP, EXCEDE, SPIRE, etc., should provide an excellent base against which the auroral code work developed during the past year may be checked. Also, other data sources, such as measurements on PCA events, should be regularly reviewed for use in this code validation. To optimize the use of such data it is suggested that, where feasible, an iterative feedback loop be established between the measurement program and the modeling or simulation effort. With such a communications link, the simulation effort can be provided with advance information on sensors to be used on experimental plans, and on operational parameters such as expected EXCEDE beam energy and spectrum. Also, the experimentalist may receive valuable input from the modeler on those elements of his measurement program which could be improved to provide more useful and usable data. Such a link could also provide for a more timely exchange of information so that the modeler is not continually working on old data.

## ACKNOWLEDGEMENT

The authors would like to acknowledge the many helpful suggestions and information received in interactions with other staff members, particularly with Dr. T. Coffey. They would also like to thank Dr. H. Linnerud for his assistance in assembling and reviewing this report.

## REFERENCES

1. P. M. Banks, C. R. Chappell, A. F. Nagy, J. Geophys. Res. 79, 1459 (1974).
2. W. L. Fite, R. T. Brackmann, Phys. Rev. 113, 815 (1959).
3. R. J. W. Henry, P. G. Burke, A. L. Sinfailam, Phys. Rev. 178, 218 (1969).
4. E. Zipf (private communication).
5. D. Rapp, P. Englander-Golden, J. Chem. Phys. 43, 1464 (1965).
6. B. L. Schran, F. J. DeHeer, M. J. vanderWiel, J. Kistenmaker, Physics 31, 94 (1965).
7. W. L. Borst, Phys. Rev. A5, 648 (1972).
8. P. N. Stanton, R. M. St. John, J. Opt. Soc. Am. 59, 252 (1969).
9. S. Chung, C. C. Lin, Phys. Rev. A6, 988 (1972).
10. T. G. Finn, J. F. M. Aarts, J. P. Doering, J. Chem. Phys. 56, 5632 (1972).
11. J. F. M. Aarts, F. J. deHeer, Chem. Phys. Lett. 4, 116 (1969).
12. A. Chutjian, D. C. Cartwright, S. Trajmar, Phys. Rev. Letters 30, 195 (1973).
13. A. E. S. Green, R. S. Stolarski, J. Atmos. Terr. Phys. 34, 1703 (1972).
14. G. J. Schulz, Phys. Rev. 135, A988 (1964).
15. D. Spence, J. L. Mauer, G. J. Schulz, J. Chem. Phys. 57, 5516 (1972).
16. F. Linder, A. Schmidt, Z. Naturforsch, 26a, 1617 (1971).
17. S. Trajmar, D. C. Cartwright, W. Williams, Phys. Rev. A4, 1482 (1971).

18. S. Trajmar, W. Williams, A. Kuppermann, J. Chem. Phys. 56, 3759 (1971).
19. P. S. Julienne, "A Continuous Slowing Down Electron Deposition Model," An NRL Memo-Report in publication.
20. D. J. Strickland, "Angular Properties and Energy Deposition of keV Electrons in the Aurora," An NRL Memo-Report in publication.
21. D. J. Strickland and P. C. Kepple, "Preliminary Report on the Transport and Production of Energetic Electrons in Auroras," NRL Memo-Report #2779, April 1974.
22. M. Walt, W. M. MacDonald, and W. E. Francis, "Penetration of Auroral Electrons into the Atmosphere," Physics of the Magnetosphere, Reidel, Holland, 1967.
23. A. Chutjian, D. C. Cartwright, S. Trajmar, Phys. Rev. Lett. 30, 195 (1973).
24. J. M. Ajello, J. Chem. Phys. 53, 1156 (1970).
25. A. E. S. Green and R. S. Stolarski, J. Atm. Terr. Phys. 34, 1703 (1972).
26. D. Rapp and P. Englander-Golden, J. Chem. Phys. 43, 1464 (1965).
27. B. L. Schram, F. J. deHeer, M. J. vanderWiel, J. Kistenaker, Physica 31, 94 (1965).
28. B. N. Srivastava, and I. M. Mirza, Phys. Rev. 176, 137 (1968).
29. S. Trajmar, D. C. Cartwright, W. Williams, Phys. Rev. A4, 1482 (1971).
30. F. Linder and A. Schmidt, Z. Naturforsch, 26a, 1617 (1971).
31. S. Trajmar, W. Williams, and A. Kuppermann, J. Chem. Phys. 56, 3759 (1971).
32. W. L. Borst and E. Zipf, Phys. Rev. A1, 1410 (1970).

33. R. J. W. Henry, P. G. Burke, and A. L. Sinfailam, *Phys. Rev.* 178, 218 (1969).
34. W. L. Fite and R. T. Brackmann, *Phys. Rev.* 113, 815 (1959).
35. F. C. Fehsenfeld, A. L. Schmeltekopf, D. B. Dunkin, and E. E. Ferguson, ESSA Tech. Rept. ERL 135-AL3, Boulder, Colo. (1969).
36. M. McFarland, D. L. Albritton, F. C. Fehsenfeld, E. E. Ferguson, and A. L. Schmeltekopf, *J. Chem. Phys.* 59, 6620 (1973).
37. J. A. Rutherford and D. A. Vroom, *J. Chem. Phys.* 55, 5622 (1971).
38. R. F. Stebbings, B. R. Turner, and J. A. Rutherford, *J. Geophys. Res.* 71, 771 (1966).
39. F. C. Fehsenfeld, D. B. Dunkin, and E. E. Ferguson, *Planet. Space Sci.* 18, 1267 (1970).
40. D. F. Strobel, private communication.
41. D. Garvin, Chemical Kinetics Data Survey V., NBSIR 73-206, May 1973.
42. Reaction Rate Handbook, Second Edition (1972).
43. W. L. Fite, *Can. J. Chem.* 47, 1797 (1969).
44. R. A. Young and G. A. St. John, *J. Chem. Phys.* 48, 895 (1968).
45. D. E. Shemansky, E. C. Zipf, and T. M. Donahue, *Planet. Space Sci.* 19, 1669 (1971).
46. I. D. Clark, and R. P. Wayne, *Chem. Phys. Letters* 3, 405 (1969).
47. E. C. Zipf, *Can. J. Chem.* 47, 1863 (1969).
48. J. E. Rogerson and J. Davis, "Preliminary Report on an Auroral Proton Deposition Study, NRL Memorandum-Report in publication.
49. L. R. Peterson, *Phys. Rev.* 187, 105 (1969).

50. S. K. Allison, Rev. Modern Phys. 30, 1137 (1958).
51. L. G. Jacchia, "Static Diffusion Models of the Upper Atmosphere with Empirical Temperature Profiles," Smithsonian Inst. Astrophys. Observ., Res. Space Sci., Spec. Report, 170, 1965.
52. E. Hyman and P. Julienne, AURORA - An NRL Auroral Chemistry Code, NRL Memo Report in publication.
53. R. A. McClatchey, R. W. Fenn, J. E. A. Selby, F. E. Volz, and J. S. Garing, AFCRL-72-0497, August 1972.
54. G. J. Schulz, Phys. Rev. 135, A988 (1964).
55. D. Spence, J. L. Mauer, and G. J. Schulz, J. Chem. Phys. 57, 5516 (1972).
56. W. L. Borst, Phys. Rev. A5, 648 (1972).
57. P. N. Stanton, R. M. St. John, J. Opt. Soc. Am. 59, 252 (1969).
58. S. Chung and C. C. Lin, Phys. Rev. A5, 988 (1972).
59. T. G. Finn, J. F. M. Aarts, J. P. Doering, J. Chem. Phys. 56, 5632 (1972).
60. J. F. M. Aarts, F. J. deHeer, Chem. Phys. Lett. 4, 116 (1969).
61. J. A. Fedder, An Ionospheric Model for Current, the Electric Field, and the Plasma Density in an Auroral Arc, NRL Memo-Report #2691, January 1 74.
62. J. G. Romick and A. E. Belon, "The Spatial Variation of Auroral Luminosity - II; Determination of Volume Emission Rate Profiles," Planet. Space Sci., 15, 1695 (1967).
63. N. C. Maynard, A. Bahnsen, P. Christopherson, A. Egeland, and R. Lundin, "An Example of Anticorrelation of Auroral Particles and Electric Fields," J. Geophys. Res., 78, 3976 (1973).
64. P. A. Cloutier, B. R. Sandel, H. R. Anderson, P. M. Pazich, and R. J. Spiger, "Measurement of Auroral Birkeland Current and Energetic Particle Fluxes," J. Geophys. Res., 78, 640 (1973).

65. W. I. Axford and C. O. Hines, "A Unifying Theory of High-Latitude Geophysical Phenomena and Geomagnetic Storms," *Can J. Phys.* 39, 1433 (1961).
66. J. P. Heppner, "The Harang Discontinuity in Auroral Belt Ionospheric Currents," *Planet. Space Sci.*, 20 (1972).
67. D. A. Gurnett and L. A. Frank, "Observed Relationships Between Electric Fields and Auroral Particle Precipitation," *J. Geophys. Res.* 78, 145 (1973).
68. J. C. Armstrong and A. J. Zmuda, "Field-Aligned Currents and Flow Directions," *EOS* 55, 393 (1974).
69. L. Harang, "The Mean Field of Disturbance of Polar Geomagnetic Storms," *Terr. Mag. Atmos. Elec.* 51, 353 (1946).
70. S-I. Akasofu, "New Morphological Features of Auroras Revealed by DAPP Photographs," paper presented at 55th Annual Mtg. of the American Geophys. Union, Washington, D. C., April 1974.
71. A. L. Snyder, S-I. Akasofu, and T. N. Davis, "Auroral Substorms Observed from above the North Polar Region by a Satellite," *J. Geophys. Res.* 79, 1393 (1974).
72. D. F. Strobel, *J. Geophys. Res.* 76, 2441 (1971).
73. Berger, M. J., S. M. Seltzer, and K. Maeda, "Some New Results on Electron Transport in the Atmosphere," *J. Atmosph. Terr. Phys.*, 36, 591, 1974.